Taneli Juntunen

Quantum transport and terahertz photoconductivity in a mesoscopic carbon nanotube film

School of Electrical Engineering

Thesis submitted for examination for the degree of Master of Science in Technology.

Espoo 9.3.2015

Thesis supervisor:

Prof. Ilkka Tittonen

Thesis advisor:

Assoc. Prof. Yukio Kawano

Aalto University
School of Electrical
Engineering

AALTO UNIVERSITY
SCHOOL OF ELECTRICAL ENGINEERING

ABSTRACT OF THE
MASTER'S THESIS

Author: Taneli Juntunen

Title: Quantum transport and terahertz photoconductivity in a mesoscopic carbon nanotube film

Date: 9.3.2015 Language: English Number of pages:9+64

Department of Micro- and Nanosciences

Professorship: Electrophysics Code: S-129

Supervisor: Prof. Ilkka Tittonen

Advisor: Assoc. Prof. Yukio Kawano

Terahertz (THz) technology has recently ascended to considerable potential, providing new attractive possibilities for basic materials research by giving access to physically fundamental energy scales. In particular, THz radiation may offer a possibility to obtain deeper understanding of electronic transport mechanisms in complex *mesoscopic* systems, which exhibit quantum fluctuations resulting from the wave character of electrons. Films of single-wall carbon nanotubes (SWCNTs) provide an especially interesting setting for such a purpose due to their phenomenal electrical and optical properties, as well as complex nature arising from the interplay between inter-tube and intra-tube transport.

This thesis investigates electronic transport and THz-induced conductivity in a macroscopically aligned ultralong SWCNT film grown by chemical vapour deposition. The aim is to establish the predominant conduction mechanisms, determine the interplay between these mechanisms and THz radiation, and assess the feasibility of using the system for THz detection.

The experimental findings show a cross-over from conduction governed by phonon-induced tunnelling processes between strongly localized states to weak localization, classified as quantum transport, as the temperature is decreased to ~ 5 K. Illuminated by 2.52 THz radiation, the device exhibits a strong polarization independent change in resistance, measured up to $\sim 55\%$ in the low temperature limit and attributed to interaction between THz radiation and localization effects.

Although the photoresponse was restricted to the low temperature regime (T=3–20 K) limiting the use of the system for efficient THz detection, the results introduce an interesting possibility that THz illumination influences the single-electron interference originated coherent backscattering effect in the presence of weak localization. Further insight into these interactions is expected to be obtained by time-domain and frequency-domain measurements.

Keywords: localization, terahertz, mesoscopic physics, VRH, scaling theory, carbon nanotube, quantum transport

AALTO-YLIOPISTO
SÄHKÖTEKNIIKAN KORKEAKOULU

DIPLOMITYÖN
TIIVISTELMÄ

Tekijä: Taneli Juntunen

Työn nimi: Kvanttikuljetusilmiöt ja terahertsifotojohtavuus mesoskooppisessa hiilinanoputkikalvossa

Päivämäärä: 9.3.2015 Kieli: Englanti Sivumäärä:9+64

Mikro- ja nanotekniikan laitos

Professuuri: Sähköfysiikka Koodi: S-129

Valvoja: Prof. Ilkka Tittonen

Ohjaaja: Apul.Prof. Yukio Kawano

Terahertsiteknologia (THz-teknologia) on viime aikoina kehittynyt merkittäväksi tutkimusalaksi tarjoten lupaavia mahdollisuuksia materiaalitieteessä fysikaalisesti kiinnostavilla energia-alueilla. THz-säteily voi potentiaalisesti tarjota lisäinformaatiota tutkittaessa elektronisia johtavuusmekanismeja mesoskooppisissa systeemeissä, joiden kvanttifluktuaatiot juontuvat elektronien aaltoluonteesta. Yksiseinäisistä hiilinanoputkista (SWCNT, single-wall carbon nanotube) koostuvat kalvot mahdollistavat näiden kuljetusilmiöiden tutkimisen erinomaisten sähköisten ja optisten ominaisuuksiensa sekä kompleksisen rakenteensa vuoksi.
Tämä opinnäytetyö tutkii varauksen kuljettajien johtavuusilmiöitä ja THz-fotojohtavuutta makroskooppisesti suunnatussa ultrapitkässä SWCNT-kalvossa, joka on kasvatettu kemiallisella kaasufaasipinnoitusmenetelmällä. Työn tavoitteena on osoittaa kalvon pääjohtavuusmekanismit, määrittää näiden mekanismien ja THz-säteilyn vuorovaikutus ja arvioida näytteen käytettävyyttä THz-havaitsemisessa.
Kokeelliset löydökset paljastavat muutoksen voimakkaasti lokalisoituneiden tilojen välisestä fononiavusteisesta tunneloitumisesta kvanttikuljetusilmiöksi lukeutuvaan heikkoon lokalisaatioon lämpötilan laskiessa ~ 5 K:iin. 2,52 THz -taajuinen säteily aiheuttaa voimakkaan polarisaatiosta riippumattoman muutoksen näytteen resistanssissa matalissa lämpötiloissa. Enimmillään $\sim$ 55 %:n mitattu suhteellinen muutos juontuu THz-säteilyn ja lokalisaatioilmiöiden vuorovaikutuksesta.
Vaikka näytteen vaste THz-säteilyyn rajoittui mataliin lämpötiloihin (T=3–20 K) rajoittaen ilmiön käyttöä tehokkaassa THz-havaitsemisessa, tulokset tuovat esiin kiinnostavan mahdollisuuden vuorovaikutuksesta THz-säteilyn ja heikossa lokalisaatiossa elektronien interferenssistä juontuvan koherentin takaisinsironnan välillä. Lisätietoa ilmiöstä on odotettavissa saatavan ajan ja taajuuden funktiona suoritettavissa jatkotutkimuksissa.

Avainsanat: lokalisaatio, terahertsi, mesoskooppinen fysiikka, VRH, skaalausteoria, hiilinanoputki, kvanttitransportaatio

Preface

While the body of this work was prepared in Aalto University, the experiments were conducted in Oda–Kawano laboratory, Quantum Nanoelectronics Research Center at Department of Physical Electronics, Tokyo Institute of Technology, during my year there as a research student. Many contributed to my work; therefore, it is my privilege to give the following acknowledgements.

I thank professor Shunri Oda for acting as my academic advisor during my stay in his laboratory, and for welcoming me as a part of his research unit. My greatest thanks go also to associate professor Yukio Kawano for including me in his research group on terahertz science, and most of all for providing me with this research subject and showing continuous interest in my work as my thesis advisor.

Special thanks to Oda–Kawano laboratory students Naoki Fujimura, Tomoyuki Hirano, and Takayoshi Kuga for the help with the measurement system. I would also like to acknowledge our American collaborators Xiaowei He, Robert H. Hauge, and Junichiro Kono of Rice University, and Christopher W. Miller from the University of North Carolina at Chapel Hill.

As for people in Aalto University, I am most grateful to professor Ilkka Tittonen for acting as the supervisor for this thesis, and the whole of his Micro and Quantum Systems research group for continuous support and stimulating feedback. I look forward to taking on future challenges with you.

Finally, it is perhaps appropriate to acknowledge my colleagues, friends, and loved ones who have taken interest in my work; especially Oskar Bodemyr, from whom came the idea of documenting this work in the form of a thesis. Most of all, however, I thank the reader, as it is essentially for you that my work did not go in vain.

Otaniemi, 9.3.2015

Taneli Juntunen

Contents

Symbols and abbreviations

Symbols

A	Probability amplitude
$\boldsymbol{A}$	Vector potential
B	Magnetic field
d	Dimension
D	Diffusion constant
e	Elementary charge
E	Energy
E_F	Fermi energy
f	Fermi function; Frequency
F	Electric field
G	Conductance
G^A	Advanced Green's function
G^R	Retarded Green's function
g	Dimensionless conductance $G/(e^2/2\hbar)$
h	Planck's constant
$\hbar$	Reduced Planck's constant $h/2\pi$
I	Current
j	Current density
k	Wave number
$\boldsymbol{k}$	Wave vector
k_B	Boltzmann constant
l	Mean free path
L	Length
L_ϕ	Coherence length
m	Effective mass
M	Number of modes
N	Number or energy states
n	Density of states; Principal quantum number
n_e	Electron density
P	Probability
r	Position; Reflection amplitude
$\boldsymbol{r}$	Position vector
R	Resistance; Reflection probability; Response; Distance
s	Critical exponent for conductivity; Scattering probability amplitude
s'	Scattering current amplitude
S	Scattering matrix; Source
t	Transmission amplitude; Overlap energy
T	Temperature; Transmission probability
$\overline{T}$	Transmission function
u	Periodic potential

U	Potential
v	Velocity
V	Voltage
W	Width
β	Beta function
δ	Kroeneckers delta; Dirac delta function
ϵ	Energy; Laser efficiency
η	Disorder strength
κ	Dielectric constant
μ	Electrochemical potential
μ_B	Bohr magneton
ν	Critical exponent for localization length
ν_{ph}	Phonon spectrum
ξ	Localization length
ρ	Resistivity
σ	Conductivity
Σ	Self-energy
τ	Lifetime of a momentum state
τ_m	Momentum relaxation time
τ_ϕ	Phase relaxation time
χ	Transverse mode wave function; Atomic orbital
ψ	Wave function
Ψ	Digamma function
ω_c	Cyclotron frequency

Operators

$\hat{c}$	Electron annihilation operator
$\hat{c}^\dagger$	Electron creation operator
D_{op}	Differential operator
H	Matrix representation of the Hamilatonian operator
$\hat{H}$	Hamiltonian operator
$[H]$	Transfer integral matrix
I	Identity operator
$[S]$	Overlap integral matrix
∇	Vector differential operator

Abbreviations

Al_2O_3	Aluminium oxide
BV	Benzyl viologen
CI	Confidence interval
CNT	Carbon nanotube
CO_2	Carbon dioxide

CO_3OH	Methanol
CVD	Chemical vapour deposition
DOS	Density of states
DC	Direct current
ES	Efros–Shklovskii
Fe	Iron
FIR	Far-infrared
GaN	Gallium nitride
h.c.	Hermitian conjugate
He	Helium
IR	Infrared
KK	Kurobe–Kamimura
LHS	Left-hand side
MR	Magnetoresistance
MIR	Middle-infrared
MWCNT	Multi-wall carbon nanotube
N_2	Molecular nitrogen
RG	Renormalization group
RHS	Right-hand side
SEM	Scanning electron microscope
SWCNT	Single-wall carbon nanotube
THz	Terahertz
VRH	Variable-range hopping
WL	Weak localization
1D	One-dimensional
2D	Two-dimensional

1 Introduction

> *"We expect to encounter fascinating and, I believe, very fundamental questions at each stage in fitting together less complicated pieces into the more complicated system and understanding the basically new types of behavior which can result."*
>
> P. W. Anderson [1]

The theory of localization was originally formulated by Anderson in his paper of 1958, titled *Absence of Diffusion in Certain Random Lattices* [2]. Anderson proposed that electronic states in a solid, extended over the whole lattice, would become spatially localized, given that the distribution of lattice site energies is large enough, thereby inducing a sufficiently high degree of disorder in the system. The presence of disorder appears for extended states as a loss of phase-coherence through multiple scattering events. For localized waves, however, disorder manifests itself as exponentially decaying electronic wave functions with increasing distance to the localized sites. The modern era of localization theory began in the 1970s through the discovery that the conductance of a finite-size block scales in a universal manner. Until this scaling approach the limit of weak disorder had been considered rather unimportant, but it was reintroduced through a new interpretation in terms of wave interference. The desire to find manifestations of these interference effects led to the emergence of *mesoscopic* physics, describing macroscopic systems, the behaviour of which could only be understood in terms of quantum mechanics. Furthermore, localization theory could now be extended to classical waves: only recently, the concept of localization has been demonstrated for light [3], microwaves [4], and acoustic waves [5]. The timeliness of the subject is reflected by its expansion to ultra-cold atoms [6], and theoretically to photonic bandgap materials [7].

Recently, localization effects have received much attention as key phenomena for understanding low-temperature electronic transport in networks of single-wall carbon nanotubes (SWCNTs). SWCNTs are quasi-one-dimensional, rolled up sheets of graphene with increasingly promising applications in electronics and material science due to their unique mechanical, electrical and optical properties [8]. Individual SWCNTs provide a platform for studying a range of quantum effects, such as ballistic transport [9], single-electron tunnelling [10], and Luttinger liquid behaviour [11], whereas collective networks of SWCNTs can be applied as novel materials for thin-film transistors [12], conductive films [13], and sensing devices [14], among others. For such sophisticated multi-functional applications, understanding electronic transport in CNT networks appears critical. However, determining the transport characteristics of complex CNT structures has proved nontrivial due to the highly complex nature of the SWCNT networks, arising from contacts between CNTs as well as defects in individual nanotubes. Four distinct conduction mechanisms have been reported in films of SWCNTs: metallic conductivity, fluctuation induced tunnelling, variable-range hopping, and weak localization. Typically, the conduction

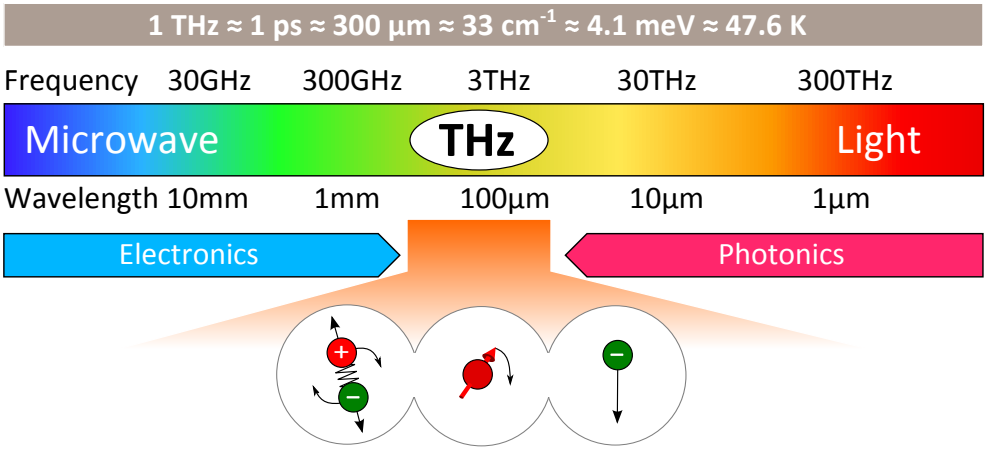

Figure 1.1: THz frequencies lie between the electronic and photonic bands of the electromagnetic spectrum. Adapted from [15, 16].

mechanism changes dynamically as the temperature of the system is varied, since localization effects are abundant only at low energy scales.

Recent progress in terahertz (THz) technology has given access to these physically fundamental energy scales, presenting great promise in solid state and condensed matter physics. The term THz technology is used to refer to the technology exploiting light in the THz (10^{12} Hz) frequency range, commonly defined as 0.3–3 THz of the electromagnetic spectrum. This corresponds to the wavelength region of approximately 0.1–1 mm, as depicted in Figure 1.1. THz frequency band connects the more well studied frequency ranges of electronics and photonics. In addition to localization energies, excitations in THz ($\sim$ meV) energy range include superconducting gaps, lattice vibrations, molecular and atomic vibrations, and spin waves [15]. Furthermore, THz technology has attracted much interest in such fields as astronomy, spectroscopy, medicine, communications, and security, where CNTs have been found promising as constituents for basic optical components [16].

However, THz induced effects have not been widely investigated in mesoscopic systems in spite of the potential of THz radiation for probing electronic transport in disordered structures and for exploiting localization effects as a strategy for THz sensing. Hence, the purpose of this thesis is to establish the electronic transport mechanisms in a mesoscopic highly aligned SWCNT film using THz radiation, and to assess the feasibility of utilizing localization effects for THz detection. This is achieved by measuring the resistance of the sample as a function of temperature both in the presence and absence of magnetic field, and by comparing these measurements with those of the THz illuminated device. The origin of the THz response is further determined by studying the THz absorption dependence of the photosignal as well as theoretical models in terms of localization theory.

Given the vast extent of our present knowledge on mesoscopic systems, a deeper description of the physics involved will not be discussed in this thesis. More advanced concepts, such as electron-electron and electron-photon interaction effects

in localization theory, remain outside the scope of this thesis. Furthermore, as the content of this thesis is weighted towards condensed matter physics, an exhaustive introduction to THz technology is not provided. More information on the current state of the research field can be found in numerous recent overviews on the subject, for example in Refs. [16, 17, 18].

This thesis is structured as follows. The theoretical foundation for analysing the experimental results of this work are provided in Chapters 2 and 3. Chapter 2 derives fundamental concepts in mesoscopic systems, whereas Chapter 3 presents localization theory, starting with a qualitative overview and a deeper look into the scaling ideas mentioned earlier. The final part of Chapter 3 describes quantitative derivation of conductivity in the strong and weak limits of localization, including the effect of magnetic field. Chapter 4 introduces carbon nanotubes, followed by a research overview on the relevant properties of CNT networks. These properties include transport characteristics as well as interaction with THz radiation. The device structure and fabrication process are explained in Chapter 5, followed by a description of THz generation and the experimental setup. Finally, experimental results and appropriate discussions are provided in Chapter 6, and Chapter 7 presents the conclusions of this thesis.

2 Quantum transport in mesoscopic systems

Conductance is the most intuitive measurable quantity to describe electronic transport in a system. The *ohmic* conductance of a macroscopic, two-dimensional conductor is classically defined as

$$G = \frac{\sigma W}{L}, \tag{2.1}$$

where σ is the conductivity, a material property, and W and L denote the width and the length of the rectangular conductor, respectively. However, as the size of the system is scaled down, several problems arise. The main problem is that electric charge is carried by electrons in discrete packages, and we should thus expect the conductance to become quantized with decreasing number of electrons. Furthermore, we cannot ignore the effect of macroscopic measuring probes on a microscopic system. The conductance is also sensitive to the non-homogeneous, atomistic structure of the material. Finally, quantum effects originating from the wave nature of electrons are not included in the macroscopic picture. In order to provide a consistent picture of electronic transport and physics at intermediate length scales between microscopic and macroscopic systems, it is therefore necessary to dismiss the classical picture of conductance and approach the problem *bottom-up*, starting from simplistic arguments based on our knowledge of quantum mechanics. Systems at these intermediate length scales are referred to as *mesoscopic*.

This chapter provides a concise description of central aspects in the field of mesoscopic physics, as they are necessary to understand the experimental work and the more subtle theoretical concepts of this thesis. The chapter consists of four sections, starting from the most simplistic possible device structure to set the fundamental basis for the theory of mesoscopic transport. The second section introduces a formulation by Landauer, which provides an intuitive picture of conductance in the presence of scattering. The third section offers a basic introduction to Green's functions, used as a language to express and connect distinct transport formalisms. In the final section, the Landauer formalism is then connected to Kubo-type conductivity by the use of Green's functions.

2.1 Preliminary concepts

In order to understand the transport phenomena present in complicated mesoscopic systems, one needs to first understand these phenomena in an elementary transistor-like device. Here, we derive the conductance for such a device structure, loosely following Ref. [19]. The structure, as illustrated in Figure 2.1a, consists of a source, connected to a drain with an electrical conductor. As a bias voltage, V, is applied between the source and the drain, the source begins to inject electrons into the conductor, from which the electrons are further collected by the drain.

In the basic *effective mass* approximation, an electron confined to the conductor is

expressed in terms of wave functions of the form

$$\psi(\mathbf{r}) = \exp(\mathrm{i}k_x x)\exp(\mathrm{i}k_y y)\exp(\mathrm{i}k_z z), \tag{2.2}$$

where each component of the wave vector $\mathbf{k}$ is quantized depending on the confinement in the respective coordinate directions:

$$k_x = \frac{n_x \pi}{L_x}, \qquad k_y = \frac{n_y \pi}{L_y}, \qquad k_z = \frac{n_z \pi}{L_z}, \tag{2.3}$$

where n_i with $i \in [x, y, z]$ is an integer. The wave number associated with $\mathbf{k}$ is defined as $k = \sqrt{k_x^2 + k_y^2 + k_z^2} = \sqrt{2mE/\hbar^2}$. For simplicity, the conductor is now considered quasi-one-dimensional in the x-direction. Thus, due to tight confinement in both y- and z-directions, the energy separation between two transverse *modes* is sufficient for only one transverse mode to exist in some small energy range under investigation.

The conductance can be obtained by first calculating the current. By dimensional analysis, the unit of current is *charge over time*. Thus, the current carried by a single electron with some wave number k equals the charge, e, multiplied by the velocity, v, of the electron and the number of electrons associated with a single energy state per unit length in the conductor, i.e. $1/L$. If multiple such states exist with different values of the wave number, the current is given by

$$I = \frac{e}{L}\sum_k v f^+(k), \tag{2.4}$$

where $f^+(k)$ is some function that determines the occupancy of the state k. We can convert this summation into an integral over energy by defining the *density of*

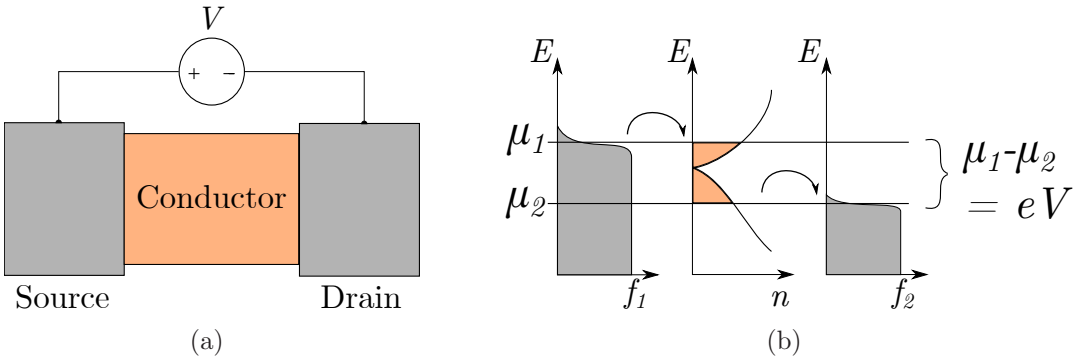

Figure 2.1: a) The investigated simplistic device structure. b) An applied voltage over the conductor displaces the system from electrochemical equilibrium and produces net current flow from the source to the drain. Adapted from [19].

states (DOS), n, as the number of energy states per unit energy and unit length. Converting the summation in Eq. 2.4, we thus obtain

$$I = \frac{e}{L} \int Lnv f^+(E) \mathrm{d}E. \tag{2.5}$$

To evaluate n, the number of filled energy states in a system of energy E can be calculated as

$$N = 2\frac{1}{2}\frac{k}{\pi/L} = \sqrt{2mE}\frac{L}{\hbar\pi} \tag{2.6}$$

following the quantization rule of Eq. 2.3. Here, spin adds the multiplicity of two, and the factor of half corrects the redundancy of counting the identical states $\pm n$ twice. DOS is then

$$n = \frac{\mathrm{d}N}{\mathrm{d}E}\frac{1}{L} = (\pi\hbar v)^{-1}, \tag{2.7}$$

where $v = \sqrt{2E/m}$. Substitution of this expression back into Eq. 2.5 yields

$$I = \frac{2e}{h} \int f^+(E) \mathrm{d}E. \tag{2.8}$$

If we expand this result to a 2D-conductor by loosening the confinement in, say, the y-direction, we can have multiple modes of transport at a single energy E. Defining the number of these modes at E as $M(E)$, the current is finally obtained as

$$I^+ = \frac{2e}{h} \int f^+(E) M(E) \mathrm{d}E. \tag{2.9}$$

Next, we discuss the function $f^+(E)$ expressing occupancy of a state at energy E. States which contribute to the current are filled by the source and emptied by the drain. With no applied voltage over the structure, both the source and the drain are in electrochemical equilibrium and no current flows. The energy states inside the source and the drain are filled according to the Fermi function

$$f(E) = \frac{1}{e^{(E-\mu)/k_B T} + 1}, \tag{2.10}$$

where μ is the *electrochemical potential*, equal to the Fermi energy, E_F, in electrochemical equilibrium. At close to zero temperature, the Fermi function represents effectively a Heaviside step function, for which all the states below μ are occupied, while none of the states above the electrochemical potential are occupied. Also the conductor is in equilibrium with the source and the drain, since it is in electrical

contact with both reservoirs. By displacing the system from equilibrium by applying a small bias voltage, V, over the structure, we induce a difference between the electrochemical potentials μ_1 and μ_2 of the source and the drain with the corresponding Fermi functions f_1 and f_2, so that

$$\mu_1 - \mu_2 = eV. \tag{2.11}$$

Now, the source tends to equilibrium by filling all the states below μ_1 in the conductor, whereas the drain tends to keep all the states above μ_2 empty, as illustrated in Figure 2.1b. These competing processes result in the flow of current.

It is therefore determined by $f_1(E)$ and $f_2(E)$ if a state contributes to current flow. Thus, the occupancy function in Eq. 2.9 can be defined as

$$f^+(E) = f_1(E) - f_2(E). \tag{2.12}$$

At zero temperature, only states between μ_1 and μ_2 conduct current. The current is then obtained as

$$I = \frac{2e}{h}\int_{\mu_2}^{\mu_1} M(E)[f_1(E) - f_2(E)]\mathrm{d}E = \frac{2e}{h}MeV. \tag{2.13}$$

Thus, the conductance is

$$G = \frac{I}{V} = \frac{2e^2}{h}M. \tag{2.14}$$

The conductance is therefore fundamentally quantized in units of $2e^2/h$. However, as we did not include any scattering effects inside the conductor in our model, Eq. 2.14 describes *ballistic* conduction at zero-temperature. Moreover, in Eq. 2.11 we assumed linear response, which is a reasonable argument only for low bias voltages. In the next section, this expression is modified to include scattering at the conductor.

2.2 Landauer formulation

The previous section derived the conductance for a simple transistor-like structure, assuming that the electrons could flow ballistically through the conductor with no scattering from, e.g., impurities. To expand our investigation to disordered structures studied in this thesis, it is necessary to evaluate the conductance in the presence of scattering.

A famous approach by Landauer expresses conductance in terms of the scattering properties of the system. It is especially suited for treating a disordered system with a simple device geometry and two contacts. Perhaps even more importantly,

it has provided physical insight and deeply evolved the general understanding of mesoscopic transport phenomena. The formulation is sometimes referred to as the transmission formulation, since it stresses the importance of equivalence between conductance and transmission [20].

We modify the structure of the previous section after Ref. [20], so that the channel of the device consists of two ideal ballistic leads separated by a conductor, as depicted in Figure 2.2. The leads can be considered semi-infinite for any practical purpose. The conductor acts now as a scatterer, characterized by the transmission probability through the scattering system, S, denoted by T, and the probability for an electron to change direction due to scattering at S, signified by R. The relation between T and R is $T = 1 - R$. It is of importance that all the scattering events are *elastic*, in that they retain the wave properties of the scattering electrons. The conductor can be thus called *coherent*.

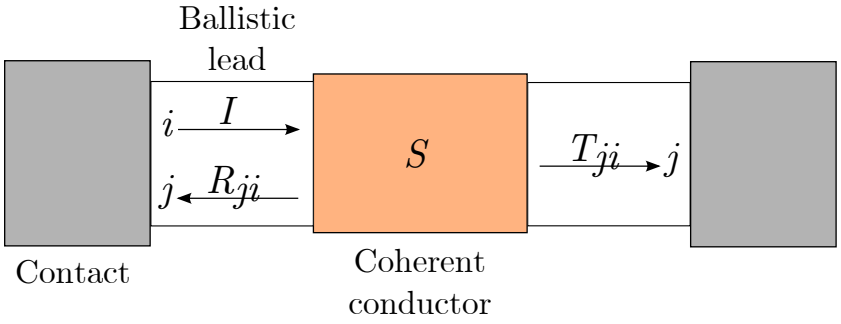

Figure 2.2: The device structure for Landauer formalism: an incoming electron, I, from the left contact reservoir is scattered by the conductor into the leads. Adapted from [20].

For simplicity, we first investigate a single-channel case, where the conduction is determined by only two modes: a mode propagating from the left to the right, and a mode propagating from right to left. Considering the transmission and reflection probabilities for a single mode, we can modify Eq. 2.13 to obtain the current in the right lead as

$$I = \frac{e}{\pi\hbar}\int_{\mu_2}^{\mu_1} \mathrm{d}E[f_1(E)T + f_2(E)R - f_2(E)] = \frac{(\mu_1 - \mu_2)e}{\pi\hbar}T. \tag{2.15}$$

Since $(\mu_1 - \mu_2) = eV$, the conductance is obtained as

$$G = \frac{I}{V} = \frac{2e^2}{h}T. \tag{2.16}$$

This is the *Landauer formula* for the single-channel case.

For the multichannel case, we consider the system composing of a collection of single channels, related to each other through scattering. Due to quantization of the

transverse modes, we now have M conducting channels close to the Fermi energy. An incoming wave from the *left-hand side* (LHS) jth channel has the probability $T_{ij} = |t_{ij}|^2$ to proceed into the *right-hand side* (RHS) ith channel and the probability $R_{ij} = |r_{ij}|^2$ to reflect backwards into the LHS ith channel. The probability amplitudes for waves coming from the RHS are denoted by primes. In this manner, we can construct the *scattering* or *S-matrix*:

$$S = \begin{pmatrix} r & t' \\ t & r' \end{pmatrix}. \tag{2.17}$$

The S-matrix is of dimension $2M \times 2M$, assuming that the number of propagating modes is the same in both leads.

It is sometimes useful to define the S-matrix elements in terms of *current amplitude*, equal to the probability amplitude multiplied by the square root of the velocity. The motivation for this is that the current associated with a scattered wave is proportional to the probability multiplied by the velocity. Thus, we denote

$$s'_{nm} = s_{nm}\sqrt{v_m/v_n}, \tag{2.18}$$

where $s_{nm} = S(n, m)$. This primed quantity should not be confused with the one used in Eq. 2.17 [21].

The total transmission and reflection probability into the ith channel is now defined as

$$T_i = \sum_j T_{ij} \quad \text{and} \quad R_i = \sum_j R_{ij}, \tag{2.19}$$

Furthermore, the relation between the two is now

$$\sum_i T_i = \sum_i (1 - R_i), \tag{2.20}$$

Both Eqs. 2.19 and 2.20 are similarly true for primed quantities, implying that

$$R'_i + T_i = 1, \quad \text{and} \quad R_i + T'_i = 1. \tag{2.21}$$

Using these relations, we can derive the current similarly to Eq. 2.15 as

$$\begin{aligned} I &= \frac{e}{\pi\hbar} \sum_i \int_{\mu_2}^{\mu_1} \mathrm{d}E[f_1(E)T_i(E) + f_2(E)R'_i(E) - f_2(E)] \\ &= \frac{(\mu_1 - \mu_2)e}{\pi\hbar} \sum_i \sum_j T_{ij}, \end{aligned} \tag{2.22}$$

once again leading to conductance of the form

$$G = \frac{2e^2}{h}\overline{T}, \tag{2.23}$$

where we defined the *transmission function*, $\overline{T}$. This is the correct generalization of the Landauer formula in the multichannel case for the two-terminal conductance.

The Landauer formula of Eq. 2.23 is evidently highly similar to that of Eq. 2.14 obtained in the previous section, but it includes the transmission probability for each mode. Thus, in general G is not quantized in the fundamental units, $2e^2/h$. The Landauer formula is of fundamental importance in mesoscopic physics, and it will be later utilized in the final section of this chapter.

2.3 Green's functions

The S-matrix formulated in the previous section provides the response at one lead due to an excitation at another. Green's function is a more powerful tool for the problem, since it provides the response at any given point of the conductor due to an excitation at any other. The full potential of Green's functions becomes apparent when considering electron-electron and electron-phonon interactions, which are outside the scope of this thesis. However, Green's functions form useful relations between different transport formalisms and provide an elegant tool for calculating conductivity corrections in phase-coherent conductors due to localization effects [21]. These corrections are later investigated in Chapter 3.

The basic mathematical properties of Green's functions are introduced in the following, after Ref. [21]. Whenever a response R is related to an excitation S by a differential operator D_{op}, i.e. $D_{op}R = S$, we can define a Green's function $G \equiv D_{op}^{-1}$, so that $R = GS$. In quantum mechanics, the transport problem is expressed as

$$[E - \hat{H}]\Psi = S, \tag{2.24}$$

where Ψ is a wave function and S represents an incident wave from one of the leads. By definition, the Green's function is thus

$$G = [E - \hat{H}]^{-1}. \tag{2.25}$$

In one dimension we can write

$$\left(E - U_0 + \frac{\hbar^2}{2m}\frac{\partial^2}{\partial x^2}\right) G(x, x') = \delta(x - x'). \tag{2.26}$$

This is similar to the Schrödinger equation apart from the source term on the RHS. Physically, the Green's function can be interpreted as the wave function at x resulting from an excitation at x'. We expect the point excitation to give rise to a wave propagating away from the point of excitation with amplitudes A^+ and A^- in the $+x$- and $-x$-directions, respectively:

$$\begin{aligned} G(x,x') &= A^+ \exp\left[\mathrm{i}k(x-x')\right]; \quad x > x', \\ G(x,x') &= A^- \exp\left[-\mathrm{i}k(x-x')\right]; \quad x < x'. \end{aligned} \tag{2.27}$$

The amplitudes can be solved from the continuity conditions: G must be continuous at $x = x'$ and, furthermore, the derivative of G must be discontinuous by factor of $2m/\hbar^2$ due to discontinuity of the Dirac delta function at $x = x'$. By solving Eqs. 2.27 with the continuity conditions, one obtains

$$A^+ = A^- = -\frac{\mathrm{i}}{\hbar v}. \tag{2.28}$$

Finally, the Green's function is acquired as

$$G(x,x') = -\frac{\mathrm{i}}{\hbar v} \exp\left[\mathrm{i}k|x-x'|\right]. \tag{2.29}$$

The solution is generally called the *retarded* Green's function and denoted by $G^R(x,x')$.

It is noteworthy that there exists another solution satisfying different boundary conditions; namely,

$$G(x,x') = +\frac{\mathrm{i}}{\hbar v} \exp\left[-\mathrm{i}k|x-x'|\right], \tag{2.30}$$

which represents incoming waves that disappear at the point of excitation. The latter solution is called the *advanced* Green's function and it is denoted by $G^A(x,x')$. The boundary conditions can be included in the expressions of $G^R(x,x')$ and $G^A(x,x')$ by adding a small positive imaginary term, $\eta \to 0^+$, into Eq. 2.25:

$$\begin{aligned} G^R &= [E - \hat{H} + \mathrm{i}\eta]^{-1}, \\ G^A &= [E - \hat{H} - \mathrm{i}\eta]^{-1}. \end{aligned} \tag{2.31}$$

The imaginary term will automatically cause the unacceptable solution to diverge to infinity and thus unphysical. It is easy to show that $G^A = (G^R)^\dagger$. In the remainder of this thesis, the retarded Green's function will be considered simply *the* Green's function.

To account for multiple modes in the leads, we simply include the transverse modes,

χ_m, by writing

$$G^R(x,x') = \sum_m A_m^{\pm}\chi_m(y)\exp\left[\mathrm{i}k_m|x-x'|\right]. \tag{2.32}$$

The transverse mode eigenfunctions are orthogonal and satisfy the Schrödinger equation independently. We further assume that they are real, which is always the case in a quantum confinement problem. To calculate the mode amplitudes A_m^+ and A_m^-, we utilize the same continuity conditions (evaluated at $y = y'$) as used for the single-moded wire to acquire

$$A_m^+ = A_m^- = -\frac{\mathrm{i}}{\hbar v_m}\chi_m(y'). \tag{2.33}$$

Thus, the Green's function for multi-moded wires is

$$G^R(x,y;x',y') = \sum_m -\frac{\mathrm{i}}{\hbar v_m}\chi_m(y)\chi_m(y')\exp\left[\mathrm{i}k_m|x-x'|\right]. \tag{2.34}$$

We end this section by addressing the problem of calculating the Green's function for an arbitrarily shaped conductor. A commonly used approach is to discretize the spatial coordinates of the system so that the differential equation of Eq. 2.31 becomes a matrix equation

$$G^R = \left[(E+\mathrm{i}\eta)I - H\right]^{-1}, \tag{2.35}$$

and $G^R(\mathbf{r},\mathbf{r'}) \rightarrow G^R(i,j)$, where i and j are points in the discrete lattice, as depicted in Figure 2.3. H is the matrix representation of the Hamiltonian operator, $\hat{H}$, and I denotes the identity matrix. The problem with inverting the matrix $[(E+\mathrm{i}\eta)I - H]$ numerically is that the semi-infinite leads of the investigated structure cause the discrete spatial lattice to be infinite. If we simply cut the leads at some point, we acquire some unwanted reflections from the newly made boundaries. Therefore, it is necessary to truncate the Green's function matrix with special care.

Our interest is to find a Green's function, G_C, describing the isolated conductor. The Green's function in Eq. 2.35 can be divided into submatrices as

$$\begin{bmatrix} G_p & G_{pC} \\ G_{Cp} & G_C \end{bmatrix} = \begin{bmatrix} (E-\mathrm{i}\eta)I - H_p & \tau_p \\ \tau_p^\dagger & EI - H_C \end{bmatrix}^{-1}, \tag{2.36}$$

where the coupling matrix τ_p is non-zero only for adjacent points in the lead p and

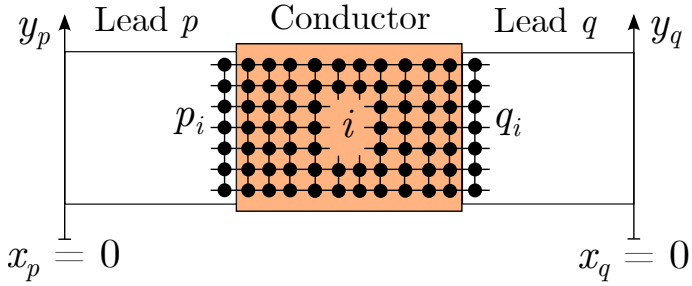

Figure 2.3: Discretizing the spatial coordinate allows describing the conductor by an isolated Hamiltonian H_C, which is connected to the leads p and q by respective coupling matrices τ_p and τ_q. p_i and q_i are points inside the leads, adjacent to the point i. Adapted from [21].

the conductor. From Eq. 2.36 we can write

$$\begin{cases} [(E+\mathrm{i}\eta)I - H_p]\, G_{pC} + [\tau_p] G_C = 0, \\ [EI - H_C]\, G_C + [\tau_p^\dagger] G_{pC} = I. \end{cases} \tag{2.37}$$

From the first equation we obtain

$$G_{pC} = -g_p^R \tau_p G_C, \qquad \text{with} \qquad g_p^R = [(E+\mathrm{i}\eta)I - H_p]^{-1}. \tag{2.38}$$

g_p^R is the Green's function for the isolated semi-infinite lead p. Substitution into the latter part of Eq. 2.37 yields

$$G_C = \left[EI - H_C - \tau_p^\dagger g_p^R \tau_p\right]^{-1}. \tag{2.39}$$

G_C is of primary relevance for electronic transport in the center of the phase-coherent conductor. All of the matrices are now finite, since the infinite lead is taken into account by the term $\tau_p^\dagger g_p^R \tau_p$. g_p^R on the other hand can be usually solved analytically for an isolated semi-infinite lead. We can thus write

$$G^R \equiv G_C = \left[EI - H_C - \Sigma^R\right]^{-1}, \tag{2.40}$$

where

$$\Sigma^R = \sum_p \Sigma_p^R \quad \text{and} \quad \Sigma_p^R(i,j) = \left[\tau_p^\dagger g_p^R \tau_p\right]_{ij}. \tag{2.41}$$

Here, we have already made clear that since G_C is our function of interest, it will be denoted as the standard retarded Green's function G^R from hereon. The term Σ^R is called *self-energy*, and it represents an effective Hamiltonian arising from the effect of

the leads on the conductor. In a general sense, self-energy provides an approximate description of not only the effect of the leads, but also effects arising from, for instance, electron–electron and electron–phonon interactions. These interactions are not in the scope of this thesis, which is why the self-energy describes the effect of the leads accurately. The usefulness of these expressions will be evident in the following section, as the Landauer formalism is connected to the so-called Kubo formalism by the use of Green's functions.

2.4 Kubo-type conductivity

Although the conductance formulated in the previous sections is derived from general considerations, the low bias limit of conductance is particularly an *equilibrium* property. Kubo formalism is based on a general theory relating low bias conductance to current fluctuations at equilibrium with no applied voltage. The main advantage of the theory is that it allows the calculation of the linear response conductivity using the methods of equilibrium statistical mechanics [23].

The Kubo formalism is generally exploited to derive the following equation for zero-temperature DC-conductivity in two dimensions, expressed using Green's functions [21]:

$$G = \frac{2e^2}{h}\frac{\hbar^2}{L^2}\sum_{\mathbf{k},\mathbf{k'}} v_x(\mathbf{k'})v_x(\mathbf{k})|G^R(\mathbf{k'},\,\mathbf{k})|^2. \tag{2.42}$$

This is an important result, as it is the starting point for calculating the weak localization conductivity corrections, as will be shown in Chapter 3. The result can be justified using Landauer transmission formalism from the earlier section. In order to do this, it is necessary to express the scattering matrix elements in the language of Green's functions. The matrix elements can then be used to calculate the transmission function in Landauer formula (Eq. 2.23).

To express the S-matrix elements using Green's functions, we once again investigate the device structure in Figure 2.3, in particular a point at $x_q = 0$ in case of an excitation at $x_p = 0$. First neglecting the transverse direction, the Green's function is

$$G^R_{qp} = \delta_{qp}A^-_p + s'_{qp}A^+_p. \tag{2.43}$$

The first term is the wave propagating in the negative x-direction, whereas the second term represents the wave travelling in the positive x-direction, scattered into different leads by the conductor. Using Eqs. 2.18 and 2.28 we then simply obtain

$$s_{qp} = -\delta_{qp} + \mathrm{i}\hbar\sqrt{v_q v_p}G^R_{qp}. \tag{2.44}$$

This relation expresses the scattering matrix elements in terms of Green's functions.

Expanding this treatment to the multi-moded case, we write

$$G^R_{qp}(y_q; y_p) = \sum_{m\in p}\sum_{n\in q}\left[\delta_{nm}A^-_m + s'_{nm}A^+_m\right]\chi_n(y_q). \tag{2.45}$$

Now using Eqs. 2.18 and 2.33 results in

$$G^R_{qp}(y_q; y_p) = \sum_{m\in p}\sum_{n\in q} -\frac{\mathrm{i}}{\hbar\sqrt{v_n v_m}}\chi_n(y_q)\left[\delta_{nm} + s_{nm}\right]\chi_m(y_p). \tag{2.46}$$

Taking advantage of the orthogonality of the transverse mode eigenfunctions, we can multiply this expression by $\chi_m(y_p)\chi_n(y_q)$ and integrate over y_p and y_q to obtain the S-matrix elements:

$$s_{nm} = -\delta_{nm} + \mathrm{i}\hbar\sqrt{v_n v_m}\int\int \chi_n(y_q)\left[G^R_{qp}(y_q; y_p)\right]\chi_m(y_p)\mathrm{d}y_q\mathrm{d}y_p. \tag{2.47}$$

This is known as the *Fisher–Lee relation* [21].

Once the Green's function has been calculated, we can use the Fisher–Lee relation to obtain the elements of the S-matrix, from which we can calculate the transmission function in the following manner. Eq. 2.47 can be expressed in the discretized space as described in the previous section for $n \neq m$ to obtain

$$\overline{T} = \sum_{n\in q}\sum_{m\in p}|s_{nm}|^2 = \sum_{i,j,j',i'}\Gamma_q(j',j)G^R(j,i)\Gamma_p(i,i')G^A(i',j'), \tag{2.48}$$

where

$$\Gamma_p(i,i') \equiv \sum_{m\in p}\chi_m(p_i)\frac{\hbar v_m}{a}\chi_m(p_{i'}). \tag{2.49}$$

The physical interpretation of Eq. 2.48 is not very straight-forward, but it is a clear representation for calculations. However, its components introduced in this chapter are conceptually important: The Green's function, G^R, represents the dynamics inside the conductor, while the self-energy, Σ^R, describes the effect of the leads. The above Γ-function signifies the coupling between the leads and the conductor.

Finally, we have the necessary tools to calculate the conductance by inserting the obtained result for the transmission function in Eq. 2.48 into the Landauer formula, $G = (2e^2/h)\overline{T}$ (Eq. 2.23). The Kubo conductance in Eq. 2.42 is expressed in the momentum space, while Eq. 2.48 was derived using a discretized real space.

However, we can transform the transmission function into k-space to obtain

$$G = \frac{2e^2}{h} \sum_{\mathbf{k}_1,\mathbf{k}_2,\mathbf{k},\mathbf{k'}} \Gamma_1(\mathbf{k}_1,\mathbf{k'}) G^R(\mathbf{k'},\mathbf{k}) \Gamma_2(\mathbf{k},\mathbf{k}_2) G^A(\mathbf{k}_2,\mathbf{k}_1). \tag{2.50}$$

The terms in the summation with $\mathbf{k}_1 = \mathbf{k'}$ and $\mathbf{k}_2 = \mathbf{k}$,

$$\Gamma_1(\mathbf{k'},\mathbf{k'}) G^R(\mathbf{k'},\mathbf{k}) \Gamma_2(\mathbf{k},\mathbf{k}) G^A(\mathbf{k},\mathbf{k'}),$$

are real, since $G^A(\mathbf{k},\mathbf{k'}) = G^R(\mathbf{k'},\mathbf{k})^*$ and Γ is Hermitian. The rest of the terms are all complex with randomly varying phases, averaging to zero to obtain

$$G = \frac{2e^2}{h} \sum_{\mathbf{k},\mathbf{k'}} \Gamma_1(\mathbf{k'},\mathbf{k'}) |G^R(\mathbf{k'},\mathbf{k}|^2 \Gamma_2(\mathbf{k},\mathbf{k}). \tag{2.51}$$

This equals to the Kubo-conductivity in Eq. 2.42 if

$$\Gamma_1(\mathbf{k},\mathbf{k}) = \Gamma_2(\mathbf{k},\mathbf{k}) = \frac{\hbar v_x(\mathbf{k})}{L}. \tag{2.52}$$

This can indeed be found to be the case by transforming Eq. 2.49 into k-space. Thus, we have found that the Landauer and Kubo formalisms are connected by Green's functions, and Eq. 2.42 is consistent with the concepts presented in the previous sections of this chapter. These ideas will be useful in the following chapter, as we calculate conductance corrections due to electron interference.

3 Localization theory

The previous chapter studied the concept of conductance in the ballistic and diffusive coherent transport regimes. The purpose of the following chapter is to investigate two important effects arising from the wave character of electrons in the diffusive regime. These *localization* effects are further classified as weak localization and strong or *Anderson* localization. The chapter consists of three sections. At first, a qualitative picture of localization effects is familiarized by illustrating the behaviour of electron waves in disordered semiconductors. The second part introduces the basic features of a scaling theory for localization, which has contributed substantially to the present understanding of these effects. Finally, a quantitative theory of conductivity is derived for weak and strong localization, using the tools provided in the previous chapter. These quantitative expressions form the basis for the analysis of the experimental data in Chapter 6.

3.1 Qualitative picture and characteristic lengths

Electron wave functions in a periodic crystal lattice are classified in terms of Bloch waves, utilized extensively to describe electronic transport and semiconductor band structures in solid state physics, and also exploited later in this thesis as the band structure of carbon nanotubes is derived in Chapter 4. Bloch waves are simply plane waves modulated by the periodic potential of the crystalline lattice and extended over the length of the structure:

$$\psi(\mathbf{r}) = \mathrm{e}^{\mathbf{ik}\cdot\mathbf{r}} u(\mathbf{r}), \tag{3.1}$$

where $u(\mathbf{r})$ is a periodic function with the same periodicity as the lattice potential. However, the crystalline states described by Bloch waves are uncommon in real structures, since generally the studied materials contain a certain degree of disorder, ranging from a few impurities to the strongly disordered limit of highly doped or amorphous structures. Disorder results in deviations from the pristine periodic potential of the lattice, thus affecting the electronic states of the system [25].

As briefly discussed in the historical review of Chapter 1, it was Anderson who first investigated the relation between disorder and electronic states. The Anderson model utilized a nearest-neighbour tight-binding model, for which the Hamiltonian can be expressed as

$$\hat{H} = \sum_i \epsilon_i \hat{c}_i^\dagger \hat{c}_i + \sum_{\langle ij \rangle} t_{ij} \hat{c}_i^\dagger \hat{c}_j + \mathrm{h.c.}, \tag{3.2}$$

where $\langle ij \rangle$ states that the atomic sites i and j are nearest neighbours, and $\hat{c}_i^\dagger$ and $\hat{c}_i$ are electron creation and annihilation operators for the ith site, respectively. Disorder can be included in the model by taking the site energy, ϵ_i, to be randomly distributed over an interval $2W$, and the overlap energy to be constant, i.e. $t_{ij} = V$.

Therefore, W/V can be considered a convenient measure of disorder in the system. In his original paper, Anderson formed a perturbation theory, or a *locator expansion*, taking the uncoupled atomic sites as the zeroth-order problem and the coupling between atoms as a perturbation. He showed that for a sufficiently high disorder, the probability for an electron positioned at an atomic site *remains* localized and will not form an extended state in a finite time. Thus, the envelope of the resulting wave function decays exponentially with increasing distance from the localized site, i.e., $|\psi(\mathbf{r})| \propto \exp\left(-|\mathbf{r}-\mathbf{r}_0|/\xi\right)$. The decay constant, ξ, is called the *localization length*. This phenomenon is referred to as strong or Anderson localization [20]. Figure 3.1 presents typical wave functions for extended and localized waves.

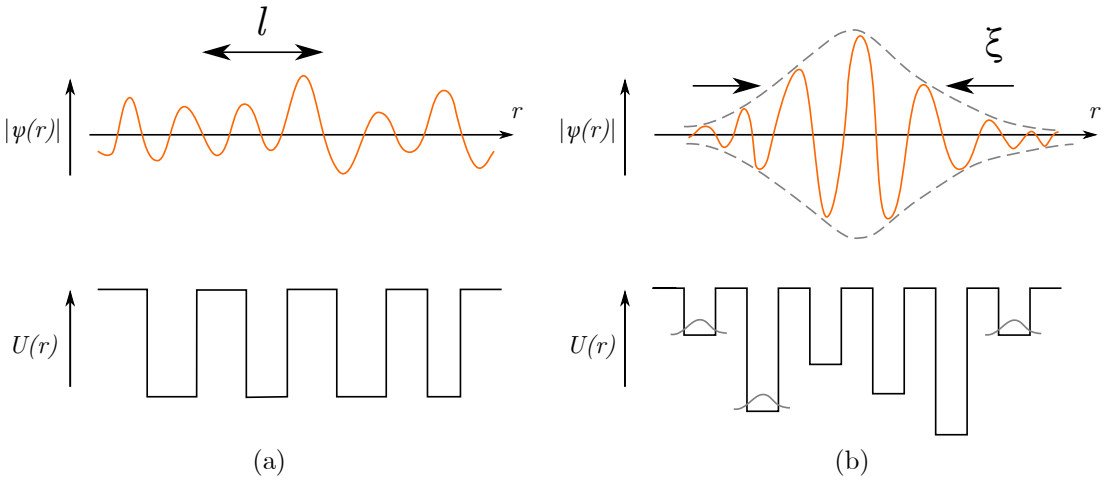

Figure 3.1: Generic wave functions for a) extended Bloch waves and b) Anderson localized waves. Anderson localization results from a high degree of disorder, manifested here as randomly varying site potentials. Adapted from [24, 25]

In keeping with the above model, it should be expected that disorder thus smears the conduction and valence band edges in a semiconductor, forming tails of localized states in the energy gap. The DOS at the tails of localized states is sufficiently low, so that the wave functions close in energy do not overlap. This introduces a band of forbidden mobilities: extended states at the conduction and valence bands are characterized by wave functions with long-range coherence in amplitude and short-range phase-coherence, while localized states beyond the abrupt *mobility edge* posses only short-range coherence both in amplitude and phase [22]. The resulting conduction properties are investigated in detail in Section 3.3.1.

Interference effects of a phase-coherent electron wave, scattered in a weak disorder, can give rise to another related localization effect; namely, weak localization. For these interference effects to occur, an electron moving in the disordered lattice must retain its phase over a *coherence length*, L_ϕ, much larger than the mean free path, l, of the electron. The respective time scales are represented by the phase relaxation time, $\tau_\phi = L_\phi/v$, and the momentum relaxation time, $\tau = l/v$. Thus, weak localization is essentially a low temperature effect, as phase-coherence is lost at high temperatures with abundant inelastic scattering. The probability for an electron to diffuse along

a path C_1 or a different path C_2 can be written in terms of respective probability amplitudes, A_1 and A_2, as $P = |A_1 + A_2|^2 = P_{cl} + P_{int}$, where $P_{cl} = |A_1|^2 + |A_2|^2$ and $P_{int} = 2\mathrm{Re}(A_1^* A_2)$. Here, the cross term P_{int} describes the wave interference between the two scattering paths. For two arbitrary paths, the interference term can be positive or negative, thus averaging to zero. However, if we consider paths returning to the original position and let C_2 be the time-reversal path of C_1, i.e. $A_1 = A_2 = A$ by time-reversal symmetry, the transition probability is enhanced by a factor of two: $P = 4|A|^2 = 2P_{cl}$. This *coherent backscattering* effect is due to constructive interference between the two paths, and it leads to reduced transmission probability, which in turn results in reduced conductivity. Coherent backscattering effect is the indicator of weak localization, and can be considered a precursor for Anderson localization [26]. The phenomenon is illustrated in Figure 3.2.

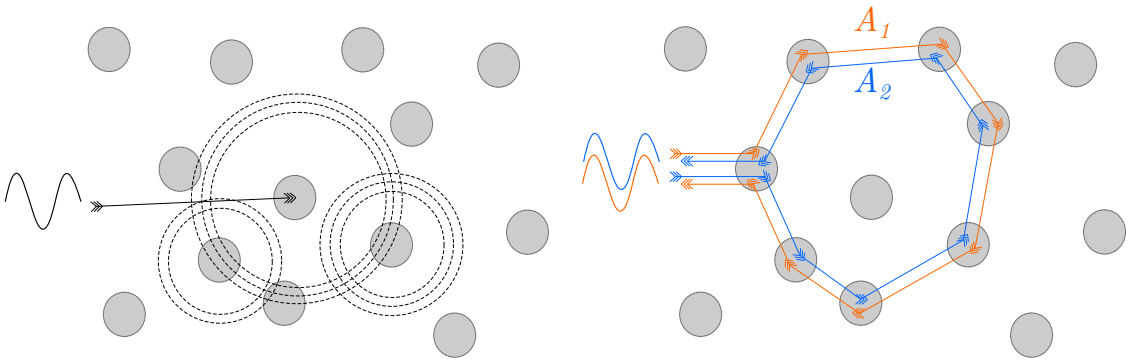

Figure 3.2: In the diffusive coherent regime, the wave properties of electrons are retained over several scattering events: a) In general, the electron has an equal probability to scatter in any direction. b) Constructive interference between a circular path and its time-reversal path leads to an increased probability for backscattering.

The reduced conductivity resulting from weak localization can be troublesome to distinguish from certain electron–electron interaction effects. However, weak localization has a characteristic sensitivity to an applied magnetic field. As an electron propagates for a circular path in a magnetic field perpendicular to its motion, the probability amplitude acquires an additional phase proportional to the line integral of the vector potential, $\mathbf{A}$, along the path: $A_1 \to A_1 \exp\left(\mathrm{i}e/\hbar \int_1 \mathbf{A} \cdot \mathrm{d}\mathbf{l}\right)$. The phase acquired by the time-reversal path, A_2, is simply negative of that acquired by A_1. Thus, an applied magnetic field destroys the time-reversal symmetry and cancels the weak localization effect [21]. Also weak localization will be quantitatively studied in the final section of this chapter.

3.2 Scaling of conductance

A scaling theory describes the behaviour of conductance as the size of the system changes. The idea of scaling theory of localization was originally put forward by

Thouless *et al.* [27], who discovered that the conductance of a finite-size block scales in a universal manner. This eventually led to a landmark paper by Abrahams *et al.* [28], arguing that the dimensionless conductance $g(L)$ obeys a *renormalization group* (RG) equation

$$\frac{\mathrm{d}\ln g}{\mathrm{d}\ln L} = \beta(g). \tag{3.3}$$

The dimensionless conductance, $g(L)$, is also known as the *Thouless number* and defined as

$$g(L) = \frac{G(L)}{e^2/2\hbar}, \tag{3.4}$$

where $G(L)$ is the conductance of a d-dimensional hypercube of length L. The denominator, $e^2/2\hbar$, is proportional to the fundamental conductance quantum discussed repeatedly in this thesis. For a good metallic conductor, conductance is expressed as $g = \sigma L^{d-2}$, where conductivity, σ, has the unit $(1/length)^{d-2}$ (see, e.g., Eq. 2.1).

An important ingredient for the RG equation was an insight by Wegner [29], according to which the Anderson localization transition should be described in the language of critical phenomena of continuous quantum phase transitions. Therefore, it is required that the correlation length ξ diverges to infinity at a critical value η_c of the strength of disorder, η:

$$\xi(\eta) \propto |\eta - \eta_c|^{-\nu}. \tag{3.5}$$

On the other hand, the conductivity is expected to tend to zero at the critical disorder, and the only characteristic length scale is expected to be the correlation length:

$$\sigma(\eta) \propto \xi^{2-d} \propto (\eta - \eta_c)^s, \tag{3.6}$$

where $\eta < \eta_c$ and $d > 2$. Here ν and s are the *critical exponents* for scaling. Now, comparing Eqs. 3.5 and 3.6, we find that $s = \nu(d-2)$. More importantly, a good metallic conductor must now have the scaling property

$$g(\eta, L) = g(L/\eta). \tag{3.7}$$

This means that g is essentially a function of a single parameter; namely L/η.

The final assumption left to justify is that the RG equation (Eq. 3.3) is independent of the strength of disorder, η, and only a function of the conductance, g. The idea is that as the size of the system changes only slightly, the change in the effective disorder is described only by it's value at the previous length scale, the only measure of this disorder being the conductance [25].

The sign of the beta function, $\beta(g)$, is of special interest, since it describes the change of conductance with increasing size of the system. At strong disorder we expect all the states to be localized exponentially with some localization length ξ, and thus

$$g(L) \propto \exp(-L/\xi). \tag{3.8}$$

In comparison with the ohmic dependence $g(L) \propto L^{d-2}$, this is strongly non-ohmic behaviour. Substituting Eq. 3.8 into the RG equation, we get

$$\beta(g) \propto \frac{\mathrm{d}(-L/\xi)}{\mathrm{d}(\ln L)} = \ln\left(\frac{g}{g_c}\right) < 1. \tag{3.9}$$

Here g_c is a pre-exponential coefficient for Eq. 3.8 in the order of unity [28]. $\beta(g)$ is evidently always negative and independent of dimensionality of the hypercube in the limit of strong disorder. This indicates that the system will eventually always be Anderson localized regardless of the dimensionality. Similarly,

$$\beta(g) = d - 2 \tag{3.10}$$

for the ohmic regime. g_c can be interpreted as a critical conductance in the sense that when $g \ll g_c$, the system obeys Eq. 3.9, and respectively when $g \gg g_c$ the system is in the ohmic regime obeying Eq. 3.10.

Our findings can now be sketched graphically as in Figure 3.3. In the three-dimensional case ($d = 3$), $\beta(g)$ is positive at large g and negative at small values of

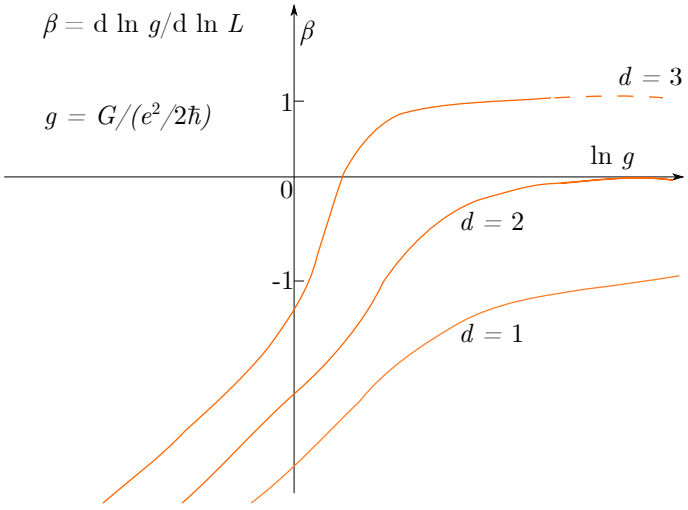

Figure 3.3: Illustration of the scaling function, β, as a function of the logarithm of the dimensionless conductance, g, in case of one-, two- and three-dimensional system. From [25].

g. Thus, it can be said that there exists a critical value of disorder, an unstable point with $\beta(g_c) = 0$, where only a small perturbation takes a large system asymptotically into metallic or insulating conduction regime. It is especially noteworthy that this being the case, the system always exhibits a *minimum metallic conductivity*. On the other hand, when $d = 1$ there exists no such transition; $\beta(g)$ is purely negative at every g and the states are, thus, localized in one dimension even with a low degree of disorder, given that the system size is sufficiently large.

The two-dimensional case ($d = 2$) appears to be special in the sense that $\beta(g) = 0$ for weak disorder. In order to determine the sign of β at large g, one has to calculate the weak localization corrections to the Drude conductivity. It turns out that β is purely negative, similarly to the one-dimensional case ($d = 1$), implying that all states are localized. However, it is now well known that even a quasi-two-dimensional system ($\mathrm{d} = 2 + \epsilon$, where $\epsilon \ll 1$) can exhibit a metal–insulator transition [26]. The weak localization corrections are investigated in the following section.

3.3 Quantitative treatment of conductivity

In order to inspect experimental data in light of localization effects, this section expands the heuristic picture of Section 3.1 in more quantitative terms. Conductivity in the strong disorder limit is characterised by tunnelling processes between spatially localized states. These processes are investigated in the first part of this section. The second part focuses on weak localization, and the necessary conductivity correction is derived by the mathematically involved diagrammatic perturbation theory. The final part of this section inspects the effect of magnetic field on conductivity in the two localization regimes.

3.3.1 Limit of strong disorder

Extensive work on conduction in the strong localization regime was done by Mott [24, 30], and the quantitative derivation here follows his original work. We consider an Anderson localized system, such as the one depicted in Figure 3.4. When the Fermi energy, E_F, lies in the energy range of the localized states, electronic conduction occurs through two distinct mechanisms. In the first mechanism, electrons are excited above the localized states, i.e. above E_C, to the conduction band. The conductivity is, thus, of the Boltzmann form

$$\sigma = \sigma_{min} \exp\left(-\frac{E_C - E_F}{k_B T}\right), \tag{3.11}$$

where σ_{min} is the minimum conductivity at $E = E_C$. This form of conduction is predominant in high temperatures when thermal excitation energy is high, and when the energy separation is small. In the second conduction mechanism the electrons hop between localized states near the Fermi energy by quantum tunnelling as also

illustrated in Figure 3.4. Three factors contribute to the tunnelling probability: a Boltzmann term $\exp(-\Delta E/kT)$, where ΔE is the energy difference between hopping sites, a factor ν_{ph} from the phonon spectrum, and a factor depending on the overlap between two wave functions. The tunnelling probability is proportional to the square of the wave function, i.e., $\exp(-2R/\xi)$ at distance R. Here, ξ is the localization length introduced in the first section of this chapter. These factors lead to two distinct hopping regimes, where the electrons tunnel either to the nearest site, referred to as *nearest-neighbour* hopping, or to a site close in energy at a variable distance, referred to as *variable-range* hopping.

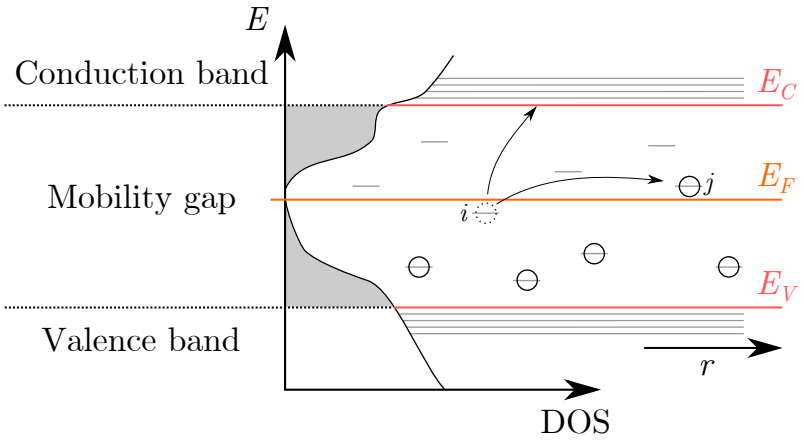

Figure 3.4: The DOS of an Anderson localized system as a function of energy, including a schematic illustration of the spatial distribution of the states. Electronic conduction in the system is governed by excitation of electrons to the conduction band or by tunnelling of the electrons between localized states near the Fermi energy.

Nearest-neighbour hopping is a common feature of strong localization, since the term $\exp(-2R/\xi)$ falls off rapidly with increasing distance. The conductivity over a range of R in the direction of the field F is constructed as follows. The number of electrons per unit volume within a thermal energy range of k_BT at the Fermi energy is $2n(E_F)k_BT$, where n is the DOS excluding spin. The hopping probabilities for these electrons in the two directions are

$$\nu_{ph} \exp\left\{-2R/\xi - \frac{\Delta E \pm eRF}{k_BT}\right\}.$$

The current density j is obtained by multiplying the difference in hopping probabilities by the unit charge e and R:

$$j = 2eRk_BTn(E_F)\nu_{ph} \exp(-2R/\xi - \Delta E/k_BT) \sinh(eRF/k_BT), \tag{3.12}$$

where the sinh function can be approximated by its argument in the case of weak

field, i.e. $eRF \ll k_BT$, to obtain the conductivity

$$\sigma = j/F = 2e^2R^2n(E_F)\nu_{ph}\exp(-2R/\xi - \Delta E/k_BT). \tag{3.13}$$

Thus, nearest-neighbour hopping conductivity manifests itself as exponential temperature dependence and is expected if $R_0/\xi \gg 1$, where R_0 is the average distance to a neighbouring site.

When R_0/ξ is comparable with or less than unity, and *always* at sufficiently low temperatures, the mechanism of variable-range hopping is to be expected, with the hopping distance, R, increasing with decreasing temperature. Now, an electron will generally hop to a site at a distance smaller than the temperature dependent R. In three dimensions, the electron has $4\pi(R/a)^3/3$ sites available for hopping, where a is the atomic spacing. It will hop to a site lowest in energy, for which

$$\Delta E = \frac{3}{4\pi R^3 n(E_F)}. \tag{3.14}$$

Similarly to the case of nearest-neighbour hopping, the hopping probability per unit time is acquired as

$$\nu_{ph}\exp\left(-2\bar{R}/\xi - \frac{\Delta E}{k_BT}\right),$$

where the average hopping distance is

$$\bar{R} = \frac{\int^R r^3\mathrm{d}r}{\int r^2\mathrm{d}r} = \frac{3R}{4}. \tag{3.15}$$

Maximizing this probability gives the optimum value for R as

$$R = \frac{3^{1/4}}{\{2\pi/\xi n(E_F)k_BT\}^{1/4}} \tag{3.16}$$

with the average hopping distance according to Eq. 3.15. Hence, by substituting the acquired $\bar{R}$ and Eq. 3.14 into the hopping probability and multiplying by $e^2n(E_F)\bar{R}^2$, we get the variable-range hopping conductivity

$$\sigma = e^2n(E_F)\bar{R}^2\nu_{ph}\exp(-B/T^{1/4}), \tag{3.17}$$

with

$$B = B_0\left\{\frac{1}{\xi^3 k_B n(E_F)}\right\}^{1/4} \quad \text{and} \quad B_0 = 2\left(\frac{3}{2\pi}\right)^{1/4} = 1.66.$$

This *Mott law* is the well established $T^{-1/4}$ dependency of variable-range hopping. It should be noted that both a constant density of states at the Fermi energy $n(E_F)$ and a temperature and distance independent phonon spectrum ν_{ph} were assumed here. Similar treatment in other dimensions allows us to generalize Eq. 3.17 for resistance as

$$R(T) = R_0 \exp\left[\left(\frac{T_0}{T}\right)^{1/(d+1)}\right], \tag{3.18}$$

where $T_0 = \beta/(k_B\xi^3 n(E_F))$ and $d = 2, 3$ is the dimensionality of the system. Here, β is a constant.

On a final remark, it is appropriate to point out a subtlety related to the case $d = 1$ in Eq. 3.18. Efros and Shklovskii [31, 32] showed that a cross-over from higher dimensional mechanism to $d = 1$ variable-range hopping is always possible due to an appearance of a *soft* gap in the DOS at the Fermi energy as follows. If an electron is excited from a state i with the energy $E_i < E_F$ to a state j with the energy $E_j > E_F$, the energy associated with the process is $E_j - E_j$ plus an additional contribution from the attractive Coulomb force between the electron at j and the newly formed hole in the state i. The energy is then lowered by the Coulombic term $-e^2/\kappa r_{ij}$, where e is the unit charge, κ is the dielectric constant and r_{ij} is the spatial separation between states i and j. We require that this transition energy is positive, so that

$$\Delta_i^j = E_j - E_i - e^2/\kappa r_{ij} > 0. \tag{3.19}$$

The form of Δ_i^j is explained by the fact that the energy of merely adding an electron to state j does not take into account the interaction between the electron-hole pair. Eq. 3.19 now indicates that states arbitrarily close to the Fermi level need to be considerably far apart. This leads to a suppression of DOS at the Fermi level, called the *Coulomb gap*.

The shape of the Coulomb gap is straight-forward to derive. If the state energies, E_i and E_j, are within ϵ from the Fermi energy, according to Eq. 3.19 the separation, r_{ij}, needs to be at least $e^2/\kappa\epsilon$. Thus, in three dimensions the spatial density of states, $n(\epsilon)$, can not be higher than $\epsilon^3\kappa^3/e^6$. The density of states $g(\epsilon) = \mathrm{d}n(\epsilon)/\mathrm{d}\epsilon$ then vanishes as ϵ^2 for vanishing ϵ. The parabolic Coulomb gap in the density of states is described as

$$g(\epsilon) = \frac{\alpha_3\epsilon^2\kappa^3}{e^6}. \tag{3.20}$$

Similar treatment yields

$$g(\epsilon) = \frac{\alpha_2|\epsilon|\kappa^2}{e^4} \tag{3.21}$$

for two dimensions. α_d is a numerical coefficient in a d-dimensional case. The Coulomb gap leads to the same Mott law as expressed in Eq. 3.18, however, with

the dimensional variable $d = 1$. Hence, d contains information on not only the dimensionality of electronic transport, but also on the DOS in the system.

3.3.2 Limit of weak disorder

The conductivity corrections in the weak disorder limit are generally derived using a diagrammatic perturbation theory, carried out here following Ref. [21], beginning from the Kubo formula for zero-temperature DC-conductivity (Eq. 2.42) introduced in Section 2.4. The Green's function formalism provides a relatively elegant presentation for the problem. Furthermore, the mathematics can be simplified by working in the momentum representation. Throughout this section, summations will be converted into integrals by $\sum_{\mathbf{k}} \Rightarrow \int \frac{\mathrm{d}\mathbf{k}}{4\pi^2}$, and while only the essential calculations are included in the following treatment, the details can be found from the aforementioned reference.

Unlike in the original Eq. 2.42, we are now interested in the *ensemble-averaged* conductivity denoted by angle brackets:

$$\sigma = \frac{2e^2}{h}\frac{\hbar^2}{L^2}\sum_{\mathbf{k},\mathbf{k}'} v_x(\mathbf{k})v_x(\mathbf{k}')\langle|G^R(\mathbf{k},\mathbf{k}')|^2\rangle. \tag{3.22}$$

This is due to the fact that the scattering potential in a two-dimensional $L \times L$ conductor under investigation can be expressed in real-space in arbitrarily many ways and, thus, we are interested in a whole ensemble of distinct conductors. The experimentally observed quantities are then ensemble-averages calculated by averaging over all phase-coherent units.

However, before discussing ensemble-averaging, the Green's function is investigated. In Chapter 2, Eq. 2.40 was derived to express the Green's function between any two points, i and j, inside the conductor. As we are mainly interested in phenomena inside a macroscopic conductor, the self-energy term Σ^R can be replaced by some imaginary $\mathrm{i}\eta_\phi$, describing the effect of environment and dephasing inside the conductor:

$$G^R = [(E - \mathrm{i}\eta_\phi)I - H_C]^{-1}. \tag{3.23}$$

Furthermore, we express the Hamiltonian inside the conductor in the momentum representation:

$$H_C(\mathbf{k}',\mathbf{k}) = \frac{\hbar^2 k^2}{2m}\delta_{\mathbf{k}',\mathbf{k}} + \underline{U}(\mathbf{k}',\mathbf{k}), \tag{3.24}$$

where

$$\underline{U}(\mathbf{k}',\mathbf{k}) = \langle \mathbf{k}' \,|\, U(\mathbf{r}) \,|\, \mathbf{k}\rangle = \int U(\mathbf{r}) \exp[-i(\mathbf{k}' - \mathbf{k})\cdot\mathbf{r}]\frac{\mathrm{d}\mathbf{r}}{L^2}. \tag{3.25}$$

To formalize this into a perturbation series, we combine Eqs. 3.23 and 3.24 to obtain the unperturbed Green's function as

$$G_0(\mathbf{k}', \mathbf{k}) = \delta_{\mathbf{k}',\mathbf{k}} \frac{1}{E - (\hbar^2 k^2/2m) + i\eta_\phi}. \tag{3.26}$$

Thus, the full Green's function including the scattering potential is given in matrix form as

$$\begin{aligned} G^R &= [G_0^{-1} - \underline{U}]^{-1} = [I - G_0\underline{U}]^{-1} G_0 \\ &= G_0 + G_0\underline{U}G_0 + G_0\underline{U}G_0\underline{U}G_0 + ... \end{aligned} \tag{3.27}$$

Defining $U_\mathbf{q} \equiv \underline{U}(\mathbf{k}', \mathbf{k})$, where $\mathbf{q} = \mathbf{k}' - \mathbf{k}$, we obtain a perturbation series of the form

$$\begin{aligned} G^R(\mathbf{k}', \mathbf{k}) =& \delta_{\mathbf{k}',\mathbf{k}} G_0(\mathbf{k}) + G_0(\mathbf{k}') U_\mathbf{q} G_0(\mathbf{k}) \\ &+ G_0(\mathbf{k}') U_{\mathbf{q}2} G_0(\mathbf{k} + \mathbf{q}_1) U_{\mathbf{q}1} G_0(\mathbf{k}) + ... \end{aligned} \tag{3.28}$$

This series can be expressed diagrammatically by *Feynman diagrams*, as depicted in Figure 3.5a. Solid line in the diagrams represent a free *propagator*, G_0, while the dashed lines denote scattering lines; namely $U_\mathbf{q}$. Complex conjugated quantities are obtained diagrammatically by reversing the arrows.

To ensemble average the perturbation series of Eq. 3.28, two simple assumptions about the character of the random scattering potential need to be made as follows. First, we assume that the scattering potential has an average value of zero. Mathematically this is expressed as $\langle U(\mathbf{r}) \rangle = 0$. Second, we assume that the scatterers are point-like and isotropic: $\langle U(\mathbf{r}) U(\mathbf{r'}) \rangle = \overline{U}^2 \delta(\mathbf{r} - \mathbf{r'})$. Now, using Eq. 3.25 we get in momentum presentation

$$\langle U_\mathbf{q} \rangle = 0 \qquad \text{and} \qquad \langle U_\mathbf{q} U_{\mathbf{q'}} \rangle = \frac{\overline{U}^2}{L^2} \delta_{\mathbf{q},-\mathbf{q'}}. \tag{3.29}$$

The perturbation series can then be ensemble-averaged term by term. As an example, a diagram with one scattering line averages to zero,

$$\langle G_0(\mathbf{k'}) U_\mathbf{q} G_0(\mathbf{k}) \rangle = 0, \tag{3.30}$$

while the diagram with two scattering lines is non-zero for $\mathbf{q}_2 = -\mathbf{q}_1$:

$$\langle G_0(\mathbf{k'}) U_{\mathbf{q}_1} G_0(\mathbf{k} + \mathbf{q}_2) U_{\mathbf{q}_2} G_0(\mathbf{k}) \rangle = \frac{\overline{U}}{L^2} G_0(\mathbf{k'}) G_0(\mathbf{k} - \mathbf{q}_1) G_0(\mathbf{k}). \tag{3.31}$$

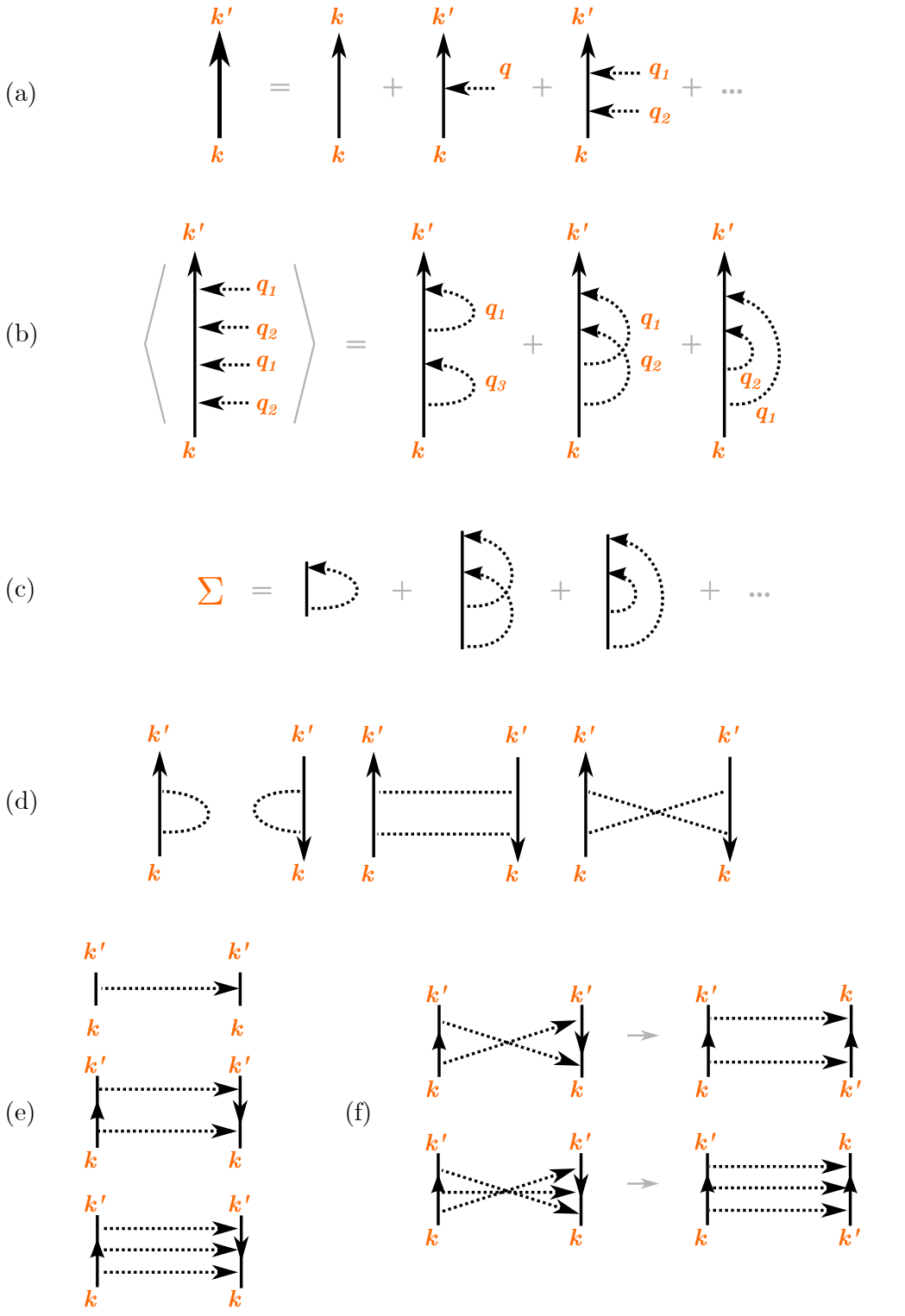

Figure 3.5: Feynman diagrams provide a pictorial representation for the diagrammatic perturbation theory: a) The perturbation series of the Green's function, G^R. b) An example of ensemble-averaging a diagram. c) The self-energy, Σ, is obtained by calculating $\langle G^R \rangle$ and leaving out the free propagators. d) An examples of a diagrammatic expressions for terms in $\langle |G^R|^2 \rangle$. e) Examples of ladder diagrams. f) Examples of maximally crossed diagrams. Compiled from [21].

Diagrammatically, ensemble-averaging thus results in connecting free scattering lines. Any diagram with an odd number of scattering lines disappears at averaging. An example of an ensemble-averaged diagram with four scattering lines is represented in Figure 3.5b, in which case the scattering lines can be connected in three ways. Since only certain diagrams contribute to the ensemble-averaged Green's function, we define a self-energy function, Σ, as a sum of all these contributing diagrams without the free propagators as depicted in Figure 3.5c:

$$\begin{aligned}\langle G^R \rangle &= G_0 + G_0 \Sigma G_0 + G_0 \Sigma G_0 \Sigma G_0 + ... \\ &= G_0 [I - \Sigma G_0]^{-1},\end{aligned} \tag{3.32}$$

which leads to the *Dyson equation*

$$\langle G^R \rangle^{-1} = G_0^{-1} - \Sigma. \tag{3.33}$$

We now have the necessary insight to evaluate the ensemble-averaged Green's function. From the scattering lines, it is elementary to see that the final momentum, **k'**, is always equal to the original momentum, **k**. The averaged Green's function is thus diagonal, so that

$$\langle G^R(\mathbf{k}, \mathbf{k'}) \rangle = \delta_{k,k'} G(\mathbf{k}). \tag{3.34}$$

This is due to the fact that the phases of the scattering matrix $U(\mathbf{k},\mathbf{k'})$ vary randomly between phase-coherent units, averaging to zero. Using Eqs. 3.26 and 3.34, we can then express the Dyson equation as

$$\frac{1}{G(\mathbf{k})} = E - \epsilon(\mathbf{k}) + \mathrm{i}\eta_\phi - \Sigma(\mathbf{k},\mathbf{k'}), \tag{3.35}$$

where $\epsilon \equiv (\hbar^2 k^2 / 2m)$.

It is noteworthy that the self-energy function, Σ, has generally both real and imaginary components, i.e. $\Sigma(\mathbf{k},\mathbf{k'}) = \sigma_{el}(\mathbf{k}) - \mathrm{i}\eta_{el}(\mathbf{k})$, so that

$$\langle G^R(\mathbf{k},\mathbf{k'}) \rangle = \delta_{\mathbf{k},\mathbf{k'}} \left(\frac{1}{E - (\epsilon + \sigma_{el}) + \mathrm{i}(\eta_\phi + \eta_{el})} \right). \tag{3.36}$$

Physically, the real part shifts the energy eigenvalues, while the imaginary part causes electrons to scatter out from the initial momentum state and, thus, the Green's function to decay with time. The decay rate of the momentum state can be shown to be

$$\frac{1}{\tau} = \frac{2}{\hbar}(\eta_\phi + \eta_{el}). \tag{3.37}$$

In the weak localization regime we must have $\eta = \eta_\phi + \eta_{el} \approx \eta_{el}$ and hence $\tau \approx \tau_{el} \ll \tau_\phi$. The elastic lifetime can be calculated to obtain the Fermi golden rule

$$\eta_{el} = \frac{\hbar}{2\tau_{el}} = \pi \overline{U}^2 n, \tag{3.38}$$

where n is the 2D-DOS excluding spin.

For calculating Eq. 3.22 we need the ensemble-average of the squared Green's function. This quantity is generally different from the squared ensemble-average of the Green's function, i.e. $\langle |G^R(\mathbf{k},\mathbf{k'})|^2 \rangle \neq |\langle G^R(\mathbf{k},\mathbf{k'}) \rangle|^2$. If one calculated the conductivity assuming these two to be the same, one would obtain an expression for the Drude conductivity:

$$\sigma_{Drude} = \frac{n_e e^2 \tau_m}{m}, \tag{3.39}$$

where n_e denotes the two-dimensional electron density. The difference thus represents the weak localization correction to the classical Drude conductivity:

$$\delta\sigma = \frac{2e^2}{h}\frac{\hbar^2}{L^2}\sum_{\mathbf{k},\mathbf{k'}} v_x(\mathbf{k}) v_x(\mathbf{k'}) \left[\langle |G^R(\mathbf{k},\mathbf{k'})|^2 \rangle - |\langle G^R(\mathbf{k},\mathbf{k'}) \rangle|^2 \right]. \tag{3.40}$$

Figure 3.5d represents an example of the diagrams obtained by calculating the first term, $\langle |G^R(\mathbf{k},\mathbf{k'})|^2 \rangle$, with diagrams of two scattering lines. However, only the first diagram in the figure belongs to the group of terms obtained by calculating $|\langle G^R(\mathbf{k},\mathbf{k'}) \rangle|^2$. Thus, the difference between the terms is represented by diagrams with scattering lines connecting $G^R(\mathbf{k},\mathbf{k'})$ to $G^R(\mathbf{k},\mathbf{k'})^*$. Such diagrams have free propagators, G, at both ends, and hence we can write

$$\delta\sigma = \frac{2e^2}{h}\frac{\hbar^2}{L^2}\sum_{\mathbf{k},\mathbf{k'}} v_x(\mathbf{k}) v_x(\mathbf{k'}) |G(\mathbf{k})|^2 |G(\mathbf{k'})|^2 \Gamma(\mathbf{k},\mathbf{k'}), \tag{3.41}$$

where the Γ-diagrams can be divided into two different categories: *ladder* diagrams and *maximally crossed* diagrams, described in Figures 3.5e and 3.5f, respectively. For isotropic scatterers, the ladder diagrams do not contribute to conductivity. The maximally crossed diagrams, however, lead to the weak localization corrections.

The physical difference between the ladder diagrams and the maximally crossed diagrams is easily captured as follows. In real space, the k-space ladder diagrams corresponding to classical transport represent the so-called *diffusons*: as a complex conjugated propagator in a diagram represents that of a hole, the ladder diagrams effectively describe electron-hole pairs propagating on a closed path in the same direction. In contrast, the maximally crossed diagrams represent an elec-

tron and a hole which move in *opposite* directions. The hole being just another electron moving around the time-reversal path, the maximally crossed diagrams denote electron–electron correlation terms, hence often called *cooperons* in reference to bound electron pairs in the theory of superconductivity. Such correlation is inevitably a quantum effect [33].

The maximally crossed diagrams can be analysed by reversing the arrow on the right in Figure 3.5f. The diagrams then form a series of the form

$$\Gamma^{(n)}(\mathbf{k},\mathbf{k'}) = \left(\overline{U}^2/L^2\right)[\Lambda(\mathbf{k},\mathbf{k'})]^n, \tag{3.42}$$

where

$$\Lambda(\mathbf{k},\mathbf{k'}) = \left(\overline{U}^2/L^2\right)\sum_{\mathbf{q}} G(\mathbf{k}-\mathbf{q})G(\mathbf{k'}+\mathbf{q})^*. \tag{3.43}$$

It is straight-forward to evaluate this geometric series as

$$\Gamma(\mathbf{k},\mathbf{k'}) = \sum_{n=1}^{\infty}\Gamma^{(n)}(\mathbf{k},\mathbf{k'}) = \frac{\overline{U}^2}{L^2}\frac{\Lambda(\mathbf{k},\mathbf{k'})}{1-\Lambda(\mathbf{k},\mathbf{k'})}. \tag{3.44}$$

Eq. 3.43 can be calculated by defining a vector $\boldsymbol{\beta} \equiv \mathbf{k}+\mathbf{k'}$ and converting the summation into an integral:

$$\Lambda(\mathbf{k},\mathbf{k'}) = \left(\overline{U}^2/L^2\right)\sum_{\mathbf{k}_1} G(\mathbf{k}_1)G(\boldsymbol{\beta}-\mathbf{k}_1)^* = \frac{\eta_{el}}{\eta}\int_0^{2\pi}\frac{1}{1+\mathrm{i}(\hbar v\beta\cos\theta/2\eta)}\frac{\mathrm{d}\theta}{2\pi}. \tag{3.45}$$

The result indicates that the contribution from the maximally crossed paths becomes important when $\boldsymbol{\beta} \equiv \mathbf{k}+\mathbf{k'} = 0$, so that $\Lambda(\mathbf{k},\mathbf{k'}) = \eta_{el}/\eta$. The maximally crossed paths thus represent unambiguously the coherent backscattering effect, qualitatively discussed in the beginning of this chapter. Following this insight, we evaluate Eq. 3.45 for small β:

$$\Lambda(\mathbf{k},\mathbf{k'}) \approx \frac{\eta_{el}}{\eta}\left(1-D\tau\beta^2\right), \tag{3.46}$$

where the standard expression for diffusion constant, $D \equiv v^2\tau/2$, and Eq. 3.37 were used. According to Eq. 3.44, $\Gamma(\mathbf{k},\mathbf{k'})$ is then

$$\Gamma(\mathbf{k},\mathbf{k'}) = (\overline{U}^2/L^2)C(\beta), \quad \text{with} \quad C(\beta) \approx \frac{1/D\tau}{(1/D\tau_\phi)+\beta^2}. \tag{3.47}$$

The approximation for $C(\beta)$ is obtained by noting that $\tau_{el} \ll \tau_\phi$ and neglecting the

β^2-term in the numerator.

Finally, we can evaluate the conductivity correction in Eq. 3.41:

$$\begin{aligned}\delta\sigma &= \frac{2e^2}{h}\frac{\hbar^2\overline{U}^2}{L^4}\sum_{\mathbf{k},\boldsymbol{\beta}} v_x(\mathbf{k})v_x(\boldsymbol{\beta}-\mathbf{k})|G(\mathbf{k})|^2|G(\boldsymbol{\beta}-\mathbf{k})|^2 C(\beta) \\ &\approx \frac{2e^2}{h}\left[\frac{\hbar^2\overline{U}^2}{L^2}\sum_{\mathbf{k}} v_x(\mathbf{k})v_x(\text{-}\mathbf{k})|G(\mathbf{k})|^2|G(\text{-}\mathbf{k})|^2\right]\frac{1}{L^2}\sum_{\beta} C(\beta).\end{aligned} \tag{3.48}$$

The term in the square brackets can be converted into an integral to obtain $-\overline{U}^2 E/4\eta^3 = -2D\tau$. Substituting this and the expression for $C(\beta)$ from Eq. 3.47 into Eq. 3.48 and converting the summation into an integral, we finally obtain

$$\begin{aligned}\delta\sigma &= -\frac{2e^2}{h}\frac{1}{2\pi}\int_0^{(D\tau)^{-1}} \frac{\mathrm{d}(\beta^2)}{\beta^2 + (1/D\tau_\phi)} \\ &= -\frac{e^2}{\pi h}\ln\frac{\tau_\phi}{\tau}.\end{aligned} \tag{3.49}$$

This is the weak localization conductivity correction in two dimensions.

The temperature dependence of the quantum mechanical correction is obtained by assuming, for instance, that $\tau_\phi \propto T^{-p}$, where p is a constant in the order of unity. The above derivation can be similarly carried out for one- and three-dimensional systems [33].

3.3.3 Effect of magnetic field

In the first section of this chapter, it was argued that a magnetic field can affect the single electron wave interference by destroying the time-reversal symmetry in a circular diffusion path and, thereby, delocalize electrons in a weakly disordered system. Experimentally, signs of VRH and weak localization are thus searched by measuring the relative change in resistance as a function of magnetic field through the sample, commonly referred to as *magnetoresistance* (MR). We end this chapter by discussing MR in experimentally verifiable terms, at both weak and strong limits of disorder.

Magnetoresistance of strongly disordered systems remains theoretically controversial, as experimental observations vary strongly between systems. Generally, the magnetoresistance of a sample in VRH regime is considered positive. Efros and Shklovskii [32] argued that magnetic field further shrinks the exponentially decaying wave function of a localized electron, reducing the overlap between adjacent hopping sites. The reduced tunnelling probability between localized sites is observed as increase in resistance as $\propto \exp B^2$. Kurobe and Kamimura [34] investigated the

effect of spin-dependent hopping in the presence of intrastate correlation. Here, a form of spin-Zeeman effect in a magnetic field reduces possible hopping sites due to Pauli exclusion principle. While there is no analytical expression for Kurobe and Kamimura type MR, the following formula reproduces the numerical results of the theory with precision [35]:

$$\frac{\Delta G}{G} = A_{KK}\frac{B^2}{B_{KK}^2 + B^2}, \tag{3.50}$$

where B_{KK} is the characteristic field for spin alignment and A_{KK} is the saturation value of the magnetoconductance. These parameters are defined in the d-dimensional case as

$$\begin{aligned} \mu_B B_{KK} &= a k_B T \left(\frac{T_0}{T}\right)^{1/(d+1)} \qquad \text{and} \\ A_{KK} &= 1 - \exp\left[-b\left(\frac{T_0}{T}\right)^{1/(d+1)}\right], \end{aligned} \tag{3.51}$$

where a and b are constants in order of unity, μ_B is the Bohr magneton, and k_B is the Boltzmann constant. On the contrary, two groups have considered the effect of interfering percolation paths through the sample, leading to negative magnetoresistance in VRH regime [36, 37, 38, 39]. The theory predicts a weak field quadratic dependence of magnetic field ($\propto B^2$), followed by a strong field linear dependence ($\propto B$).

While MR lacks consistent theoretical framework in the Anderson localized regime, the theory for weak localization regime has been highly successful. The result can be directly expanded from the theoretical treatment of the previous section [21]. Magnetic field forces electrons to propagate on a cyclical orbit. An integer number of wavelengths need to fit into a cyclotron orbit, which leads to quantization of the allowed wave vectors in the magnetic field. The corresponding allowed energy levels are called *Landau levels*, with energies same as for a quantum harmonic oscillator:

$$\frac{\hbar k_n^2}{2m} = \left(n + \frac{1}{2}\right)\hbar\omega_c \Rightarrow k_n^2 = \left(n + \frac{1}{2}\right)\frac{2eB}{\hbar}. \tag{3.52}$$

The *cyclotron frequency* is defined as $\omega_c = qB/m$. In the magnetic field all the $\mathbf{k}$-vectors are replaced with $\mathbf{k} + (e\mathbf{A}/\hbar)$, where $\mathbf{A}$ is the vector potential. Due to the fact that $\boldsymbol{\beta}$ is a sum of two $\mathbf{k}$-vectors, it is instead replaced by $\boldsymbol{\beta} + (2e\mathbf{A}/\hbar)$. The quantized β is thus expressed as

$$\beta_n^2 = \left(n + \frac{1}{2}\right)\frac{4eB}{\hbar}. \tag{3.53}$$

Evaluating Eq. 3.49 in the presence of a magnetic field we get

$$\delta\sigma = -\frac{2e^2}{h}\frac{1}{2\pi}\frac{4eB}{\hbar}\sum_{n=0}^{a}\frac{1}{\beta_n^2 + (1/D\tau_\phi)} = -\frac{e^2}{\pi h}\sum_{n=0}^{a}\frac{1}{\left(n+\frac{1}{2}\right)+b}, \\ \text{where} \quad a \equiv \frac{\hbar}{4eBD\tau} \quad \text{and} \quad b \equiv \frac{\hbar}{4eBD\tau_\phi}. \tag{3.54}$$

The sum over n can be evaluated in terms of *digamma functions*, Ψ, as

$$\begin{aligned}\delta\sigma &= -\frac{e^2}{\pi h}\left[\Psi\left(\frac{1}{2}+\frac{\hbar}{4eBD\tau}\right) - \Psi\left(\frac{1}{2}+\frac{\hbar}{4eBD\tau_\phi}\right)\right] \\ &\approx \frac{e^2}{\pi h}\left[\Psi\left(\frac{1}{2}+\frac{1}{x}\right) + \ln x\right]\end{aligned} \tag{3.55}$$

where $x = L_\phi^2 4eB/\hbar$. In the approximation we have replaced the first digamma function by its large argument limit [40]. The correction is a monotonically decreasing function of B. Thus, the magnetic field indeed induces delocalization through breaking of the time-reversal symmetry between equivalent circular scattering paths. This result in two-dimensions will be used for data analysis later in Chapter 6.

4 Carbon nanotubes

This chapter introduces the basic physical features of carbon nanotubes (CNTs), as the device structure under investigation in the experimental section consists of CNTs. The chapter is divided into two sections. The first section derives the band structure of CNTs, since majority of their unique properties can be explained in terms of the electronic structure. The latter section introduces the properties of networks of single-wall carbon nanotubes, which can portray radically different characteristics while retaining some of the unique features of individual carbon nanotubes. In the whole of this chapter, only the properties relevant to this work are presented, while more detailed description of the physical properties of CNTs and their device applications can be found in, e.g., Refs [8, 41, 42].

4.1 Band structure

Carbon nanotubes are quasi-one-dimensional, rolled up sheets of graphene. Thus, much of their electronic properties can be understood in terms of the bandstructure of the two-dimensional allotrope, graphene. The structure of graphene is illustrated in Figure 4.1a. It is a one atom thick planar sheet of sp^2-bonded carbon atoms in a hexagonal honeycomb crystal lattice [41]. The lattice consists of two triangular sub-lattices, A and B, for which the unit cell consists of two atoms. The unit vectors of the sub-lattices, A and B, are denoted by

$$\mathbf{a}_1 = \frac{a_0}{2}(3, \sqrt{3}) \equiv (a, b), \qquad \mathbf{a}_2 = \frac{a_0}{2}(3, -\sqrt{3}) \equiv (a, -b). \tag{4.1}$$

The corresponding vectors in the reciprocal k-space are then

$$\begin{aligned} \mathbf{A}_1 &= \frac{2\pi(\mathbf{a}_2 \times \hat{z})}{\mathbf{a}_1 \cdot (\mathbf{a}_2 \times \hat{z})} = \frac{2\pi}{a_0}\left(\frac{1}{3}, \frac{1}{\sqrt{3}}\right) \equiv \left(\frac{\pi}{a}, \frac{\pi}{b}\right), \\ \mathbf{A}_2 &= \frac{2\pi(\hat{z} \times \mathbf{a}_1)}{\mathbf{a}_2 \cdot (\hat{z} \times \mathbf{a}_1)} = \frac{2\pi}{a_0}\left(\frac{1}{3}, -\frac{1}{\sqrt{3}}\right) \equiv \left(\frac{\pi}{a}, -\frac{\pi}{b}\right). \end{aligned} \tag{4.2}$$

Using these vectors, we can construct the reciprocal lattice of graphene in the k_x–k_y plane and define the first Brillouin zone for the allowed $\mathbf{k}$ vectors, as depicted in Figure 4.1b. The first Brillouin zone is determined by bisecting lines connecting the origin to the closest points in the reciprocal lattice by perpendicular lines, forming an inclosed area [19].

The band structure of graphene is calculated here approximatively in terms of nearest-neighbour tight-binding model, loosely following Ref. [43]. In this approach, the wavefunctions in the solid are based on a superposition of Bloch states, formed from isolated atomistic wavefunctions located at each atomic site. To study carbon allotropes, one has to consider four atomic orbitals per atom: $2s$, $2p_x$, $2p_y$ and

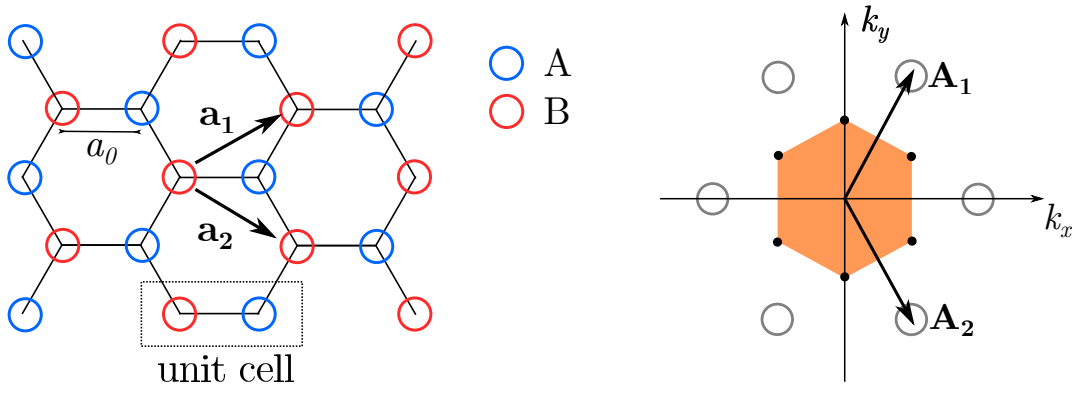

(a) (b)

Figure 4.1: The lattice structure of graphene in a) real space and b) reciprocal space. The highlighted area forms the first Brillouin zone. Adapted from [19].

$2p_z$. However, the electrical properties around and well above the Fermi energy are determined by the out-of-plane p_z orbital.

Thus, a carbon atom at $\mathbf{r}_s$ of the sub-lattice s has an unsaturated $2p$-orbital, represented by a wave function $\chi_{\mathbf{r}_s}$. We take advantage of the nearest-neighbour approximation, neglecting interactions between atoms unless the atomic sites are adjacent to each other:

$$\begin{aligned} \left\langle \chi_{\mathbf{r}_A} \middle| \hat{H} \middle| \chi_{\mathbf{r}_A} \right\rangle &= \left\langle \chi_{\mathbf{r}_B} \middle| \hat{H} \middle| \chi_{\mathbf{r}_B} \right\rangle = \epsilon_0, \\ \left\langle \chi_{\mathbf{r}_A} \middle| \hat{H} \middle| \chi_{\mathbf{r}_B} \right\rangle &= \left\langle \chi_{\mathbf{r}_B} \middle| \hat{H} \middle| \chi_{\mathbf{r}_A} \right\rangle = \gamma \delta_{|\mathbf{r}_A - \mathbf{r}_B| = a_0}, \end{aligned} \tag{4.3}$$

where ϵ_0 is the on-site energy and γ is the coupling constant. Furthermore, we neglect any overlap between orbitals, i.e., the orbitals satisfy the orthogonality relation $\left\langle \chi_{\mathbf{r}_s} \middle| \chi_{\mathbf{r}_{s'}} \right\rangle = \delta_{ss'}$. The wave function associated with the sub-lattice s can then be constructed as a Bloch wave

$$|s\mathbf{k}\rangle = \frac{1}{\sqrt{N}} \sum_{\mathbf{r}_s}^{N} e^{i\mathbf{k}\cdot\mathbf{r}_s} |\chi_{\mathbf{r}_s}\rangle . \tag{4.4}$$

Eigenfunctions in the lattice are presented as superpositions of these Bloch waves:

$$|\mathbf{k}\rangle = \sum_s C_{s\mathbf{k}} |s\mathbf{k}\rangle . \tag{4.5}$$

Substitution into Schrödinger equation, $E\left|\mathbf{k}\right\rangle = \hat{H}\left|\mathbf{k}\right\rangle$, yields

$$E\sum_{s} C_{s\mathbf{k}}\left|s\mathbf{k}\right\rangle = \sum_{s} C_{s\mathbf{k}}\hat{H}\left|s\mathbf{k}\right\rangle \Leftrightarrow E\sum_{s}\left\langle s'\mathbf{k}\right|\left.s\mathbf{k}\right\rangle C_{s\mathbf{k}} = \sum_{m}\left\langle s'\mathbf{k}\right|\hat{H}\left|s\mathbf{k}\right\rangle C_{s\mathbf{k}}, \tag{4.6}$$

which can be presented in matrix form

$$E[S]\{C\} = [H]\{C\}, \tag{4.7}$$

where square brackets and curly brackets denote matrices and column vectors, respectively. $[H]$ is called the *transfer integral matrix* and $[S]$ is called the *overlap integral matrix*, with matrix elements defined by $[H]_{s's} = \left\langle s'\mathbf{k}\right|\hat{H}\left|s\mathbf{k}\right\rangle$ and $[S]_{s's} = \left\langle s'\mathbf{k}\right|\left.s\mathbf{k}\right\rangle$. It then follows that for solving the eigenenergies, one has to solve the matrix elements of $[H]$ and $[S]$.

First solving the elements of $[H]$:

$$[H]_{AA} = \left\langle A\mathbf{k}\right|\hat{H}\left|A\mathbf{k}\right\rangle = \frac{1}{N}\sum_{\mathbf{r}_A=\mathbf{r}'_A}^{N}\left\langle \chi_{\mathbf{r}_A}\right|\hat{H}\left|\chi_{\mathbf{r}_A}\right\rangle = \epsilon_0, \tag{4.8}$$

and

$$\begin{aligned}[H]_{AB} = \left\langle A\mathbf{k}\right|\hat{H}\left|B\mathbf{k}\right\rangle &= \frac{1}{N}\sum_{\mathbf{r}_A}^{N}\sum_{\mathbf{r}_B}^{N} e^{i\mathbf{k}\cdot(\mathbf{r}_B-\mathbf{r}_A)}\left\langle \chi_{\mathbf{r}_A}\right|\hat{H}\left|\chi_{\mathbf{r}_B}\right\rangle \\ &= -\gamma(e^{i\mathbf{k}\cdot\mathbf{R}_{A1}} + e^{i\mathbf{k}\cdot\mathbf{R}_{A2}} + e^{i\mathbf{k}\cdot\mathbf{R}_{A3}}) \equiv -\gamma f(\mathbf{k}).\end{aligned} \tag{4.9}$$

$\mathbf{R}_{Ai}$ denote the nearest neighbour vectors

$$\mathbf{R}_{A1} = a_0(-1,0), \quad \mathbf{R}_{A2} = \frac{a_0}{2}(1,\sqrt{3}), \quad \mathbf{R}_{A3} = \frac{a_0}{2}(1,-\sqrt{3}). \tag{4.10}$$

Substituting $\mathbf{R}_{Ai}$ into $f(\mathbf{k})$ yields

$$f(\mathbf{k}) = e^{-ik_x a_0} + 2e^{ik_x a_0/2}\cos\left(\frac{\sqrt{3}k_y a_0}{2}\right). \tag{4.11}$$

Due to the equivalence of sub-lattices A and B, $[H]_{AA} = [H]_{BB}$. Furthermore, the Hamiltonian operator is Hermitian and, hence, $[H]_{AB} = [H]^*_{BA}$. Similarly, solving

the elements in [S] yields

$$[S]_{AA} = \langle A\mathbf{k} \,|\, A\mathbf{k} \rangle = \frac{1}{N} \sum_{\mathbf{r}_A = \mathbf{r}'_A}^{N} \langle \chi_{\mathbf{r}_A} \,|\, \chi_{\mathbf{r}_A} \rangle = 1, \tag{4.12}$$

$$[S]_{AB} = \langle A\mathbf{k} \,|\, B\mathbf{k} \rangle = \frac{1}{N} \sum_{\mathbf{r}_A}^{N} \sum_{\mathbf{r}_B}^{N} e^{i\mathbf{k}\cdot(\mathbf{r}_B - \mathbf{r}_A)} \langle \chi_{\mathbf{r}_A} \,|\, \chi_{\mathbf{r}_B} \rangle = 0. \tag{4.13}$$

Hence, it is straight-forward to see that $[S]$ is the identity matrix.

Finally, the *secular equation* is solved to obtain the energy eigenvalues:

$$\begin{aligned} &\det([H] - E[S]) = \begin{vmatrix} \epsilon_0 - E(k) & -\gamma f(k) \\ -\gamma f(k)^* & \epsilon_0 - E(k) \end{vmatrix} = 0 \\ \Leftrightarrow \quad &E(k) = \epsilon_0 \pm \gamma \sqrt{1 + 4\cos k_x a \cos k_y b + 4\cos^2 k_y b}. \end{aligned} \tag{4.14}$$

The electrons fill up exactly half of the states. We see that the energy levels are symmetrically distributed around ϵ_0, so that all the states beyond $E = \epsilon_0$ are occupied, whereas the states above are unoccupied, i.e., ϵ_0 is the Fermi energy [19]. For convenience, we now set ϵ_0 equal to 0. The obtained electronic structure for graphene is presented in Figure 4.2.

The band structure of CNTs can be obtained by taking into account the periodic boundary condition in the direction of a circumferential vector

$$\mathbf{c} = m\mathbf{a}_1 + n\mathbf{a}_2 = \hat{x}(m+n)a + \hat{y}(m-n)b, \tag{4.15}$$

so that

$$\mathbf{k} \cdot \mathbf{c} = k_x a(m+n) + k_y b(m-n) = 2\pi\nu, \tag{4.16}$$

where ν is an integer. This simply indicates returning to the same position and phase after moving around the nanotube wall. Eq. 4.16 defines lines in the k_x–k_y plane, which slice the two-dimensional graphene band structure in Figure 4.2 to form the one-dimensional bands of CNTs [42].

In order for a CNT to have zero bandgap, there must exist a state at the Fermi level. It is simple to see that $E(k) = 0$ at the six corners of the Brillouin zone. However, as they can be divided into two groups of three corners separated by reciprocal vectors, where each of the three corners constitute *one third* of a valley, it is enough to investigate only one point from both groups:

$$(k_x a, k_y b) = (0, \pm 2\pi/3). \tag{4.17}$$

Therefore, the boundary condition of Eq. 4.16 has to be met at $(k_x a, k_y b) = (0, \pm 2\pi/3)$, where $E = 0$. Substitution into equation 4.16 yields

$$(m - n)/3 = \nu. \tag{4.18}$$

Nanotubes satisfying this condition are thus metallic. The band gap is, hence, strongly dependent on the way in which the plane of graphene is rolled, often referred to as *chirality* [42].

As majority of the growth methods for single-wall carbon nanotubes (SWCNTs) have poor control over chirality, approximately 1/3 of the as-grown CNTs tend to express metallic, zero-bandgap features, while the rest of the nanotubes are semiconducting species in accordance with Eq. 4.18. Multi-wall carbon nanotubes (MWCNT), consisting of multiple nested SWCNTs, are likely to include at least one metallic SWCNT, for which MWCNTs are generally metallic [8].

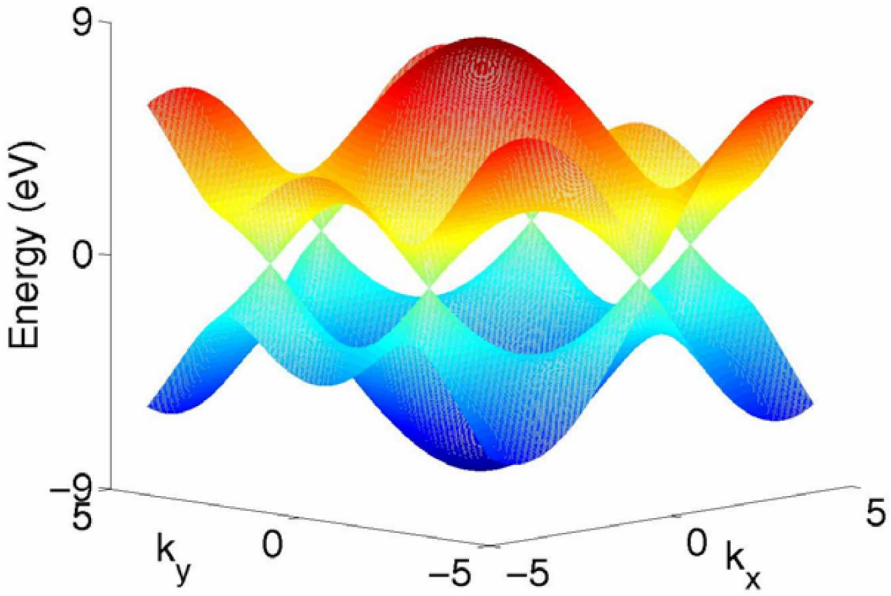

Figure 4.2: The elecronic structure of graphene, calculated by the nearest-neighbour tight-binding method. The periodic boundary condition around a CNT's wall determines parallel lines in the k_x–k_y plane, which slice the graphene band structure to form the one-dimensional energy bands of the CNT. From [42].

4.2 Single-wall carbon nanotube networks

Although the majority of research on CNTs has gone into devices using individual nanotubes as active elements, realistic technology applications are likely to incorporate networks of CNTs. The term SWCNT network refers to a range of nanostructures, fabricated by a variety of solution or chemical vapour deposition

(CVD) based methods. Networks of nanotubes avoid several problems of using single CNTs: as statistical ensembles, CNT networks have a small device-to-device variation, large active areas, high current outputs, and less sensitivity to spatial positioning in the device [44]. SWCNT networks tend to preserve or even amplify some of the unique properties of SWCNTs, while for instance charge transport can vary radically between structures depending on the orientation and contact geometries between individual SWCNTs. The following two sections introduce the main transport properties of SWCNT films, as well as the THz photoeffects observed in these structures.

4.2.1 Transport characteristics

The electronic properties of CNT networks are dominated not only by the characteristics of individual nanotubes, but also the size dependent junction resistances between CNTs [45]. Determining the electronic transport mechanism is in general highly non-trivial, since different transport mechanisms are abundant only at certain characteristic length scales and may vary as the temperature of the system changes. Generally, two main strategies are applied simultaneously to investigate the transport properties: measuring the resistance of the sample as a function of temperature, and measuring the magnetoresistance of the sample in order to find signs of localization effects. Through research on different SWCNT film structures by a number of research groups, the transport characteristics have varied between four distinct mechanisms: metallic conductivity, fluctuation-induced tunnelling (FIT), variable-range hopping and weak localization. Trivially, metallic characteristics are typical at room temperature due to high thermal energy.

The fluctuation-induced tunnelling mechanism has been found accurate in describing charge transport generally at the intermediate temperature region between metallic conductivity and variable-range hopping [46, 47]. Established by Sheng [48], FIT describes a variety of disordered materials, where the conduction electrons are delocalized and free to move over distances relatively large as compared to atomistic length scales. These materials include doped organic semiconductors, conductor–insulator composites, and amorphous materials. The conduction is then governed by electron tunnelling across the insulating barriers between the conductive regions. As the tunnel junctions separating these regions at the points of closest approach are usually small, they are subject to large thermally activated voltage fluctuations across the junction. These fluctuations affect the effective tunnelling barrier and therefore induce an additional temperature dependency to the tunnelling probability. The resistivity is, thus, of the exponential form

$$\rho \propto \exp\left(\frac{T_1}{T + T_0}\right), \tag{4.19}$$

where T_0 and T_1 are characteristic constants for the system. Since T_0 is additive to T, it is the temperature above which the fluctuations become significant. T_1/T_0

determines the tunnelling probability in the absence of fluctuations.

The VRH mechanism, introduced in Section 3.3.1, is a common feature of SWCNT films due to high degree of disorder arising from the intertube contacts and intratube defects. However, the dimension of VRH (see Eq. 3.18) conduction in SWCNT films has been shown to have little correlation with the actual device dimensions. Yanagi *et al.* [49] showed that in randomly oriented networks of CNTs, the VRH dimension is affected by the relative content of metallic nanotubes in the sample, similarly to conducting polymers [50, 51]. Pint *et al.* [52] demonstrated that, in the case of highly aligned carbon nanotubes, the transport dimension is also affected by the direction of the current relative to the nanotube alignment direction.

Finally, only a few observations of the presence of weak localization in SWCNT networks have been reported. Kim *et al.* [53] observed low-field negative MR in low temperatures in randomly oriented SWCNT networks, proposing that the behaviour may result from the coexistence of weak localization and VRH mechanisms. On the other hand, Yanagi *et al.* [49] found that weak localization became observable only as the relative content of metallic nanotubes in the sample was high.

4.2.2 Terahertz photoeffects

As basic optical components in THz technology still remain undeveloped, CNTs have received considerable attention as constituents for THz detectors. This is largely due to the exceptionally broad absorption peak of carbon nanotubes in the THz frequency range of the electromagnetic spectrum, as well as intrinsic polarization dependency resulting from the quasi-1D structure.

The origin of the strong THz aborption peak has been a controversial matter among researchers. Recently, Zhang *et al.* [54] disproved the earlier curvature-induced band gap theory and found partial support for plasma resonance theory. The plasmonic response is due to finite lengths and thus explains the strong absorptivity in the direction parallel to the quasi-1D nanotubes. Furthermore, it has been shown by the same group that the effect is further enhanced by collective antenna effects in highly aligned carbon nanotube arrays [55]. The absorption spectrum of a highly aligned SWCNT films in the THz and infrared (IR) regions is depicted in Figure 4.3.

The proposed strategies for THz detection with CNT films are commonly based on one of three photoeffects: the bolometric effect, photon induced tunnelling, and the photothermoelectric effect. The bolometric effect relies on the THz absorption properties of the lattice. Lattice heating through THz absorption induces phonons, which dissipate their energy to electrons. The bolometric effect is thus detected as a change in the conductivity of the material, i.e., photoconductivity. As a thermal effect, the detection speed is fairly slow (order of ms in low temperatures)[16].

Photon induced tunnelling is a process independent of the absorption properties of the material. The incident THz radiation consisting of individual photons can excite electrons, localized due to tight confinement to the structure or high degree of disorder. An electron can overcome the confinement potential by the excitation

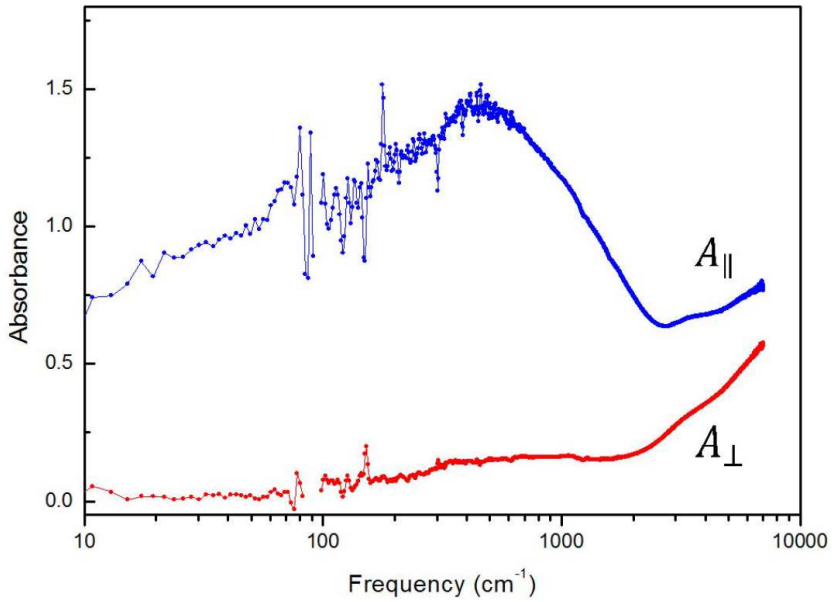

Figure 4.3: THz-IR absorbance of CVD-grown highly aligned SWCNT films parallel ($A_{||}$) and perpendicular ($A_{\perp}$) to the nanotube alignment direction. From [54].

energy and tunnel over to a new site. The tunnelling events between the localized states contribute to the overall conductivity, producing a similar signal to phonon mediated photoconductivity. However, the speed of the effect is faster, as the energy has no intermediate states between a THz photon and the electron [46, 47].

Finally, a recent development in the field has been photothermoelectric THz detection in a SWCNT film with a p–n junction formed by chemical doping [56, 57, 58]. Incident THz radiation is focused to the p–n junction, producing a temperature gradient from the junction towards the electrodes. This temperature gradient drives electrons in the n-type films and holes in the p-type film from near the junction towards the electrodes, thus inducing a voltage difference. This thermoelectric phenomenon is the *Seebeck effect*, a direct conversion of temperature into voltage. The same device structure is utilized in the experiments of this thesis, and the device is described in more detail in the following chapter.

5 Materials and methods

This chapter begins the experimental section of this thesis. It provides a brief overview of the investigated device structure and fabrication process, the used THz generation scheme, and the experimental setup utilized for studying the transport mechanisms in the device.

5.1 Device structure and fabrication

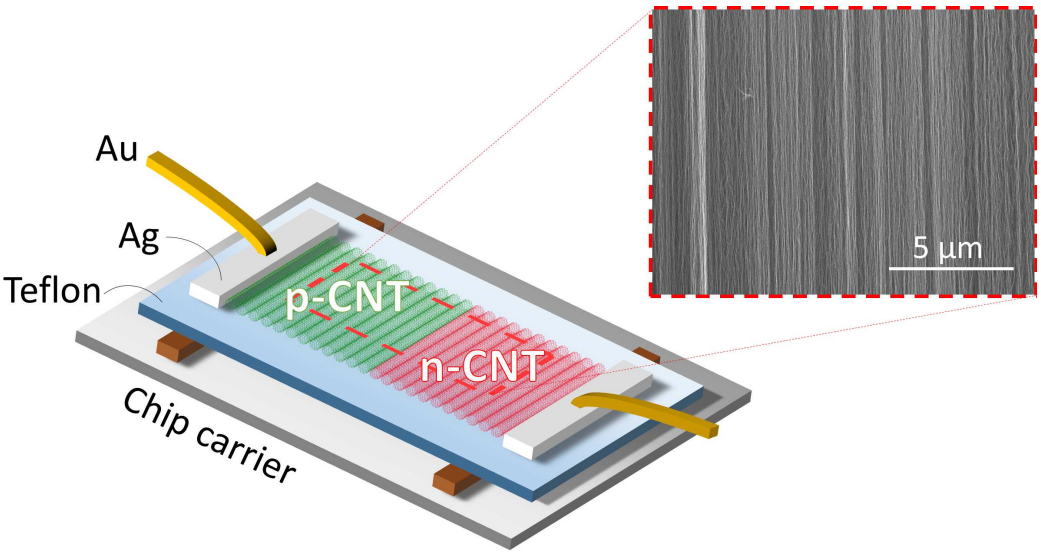

Figure 5.1: Device structure with a scanning electron microscope image of the aligned SWCNT film from previous work [56].

The device structure investigated in this thesis is illustrated in Figure 5.1, together with a scanning electron microscope (SEM) image of the device. The device is a macroscopic film of aligned, ultralong SWCNTs. About 1/3 of the SWCNTs are metallic species, while the rest 2/3 are semiconducting, although all the nanotubes are naturally p-doped by molecular adsorbates. The structure was fabricated and characterized by collaborators in Rice university as described in Refs. [56, 57, 58].

In short, the fabrication process starts by first growing CNTs vertically from a line of catalyst particles on a silicon substrate by chemical vapour deposition (CVD) [59]. The catalyst particles consisted of a 10 nm layer of aluminium oxide (Al_2O_3) and a 1 nm layer of iron (Fe), both deposited by electron-beam evaporation. After the growth, the CNTs were detached by etching and transferred onto a Teflon substrate to form a horizontally aligned macroscopic CNT film and placed on a chip carrier. The alignment of the individual CNTs was chosen to be perpendicular to the direction of electronic conduction in the measurements. The resulting film thickness was approximately 1 µm, and the width and the length of the film were determined to be 150 µm and 3 mm, respectively. Silver paste contacts were made on both ends of the film, and a p–n junction was formed in the middle of the film by

chemically doping one half of the as-grown p-type film into an n-type region with benzyl viologen (BV). Finally, gold wires were attached to the silver paste contacts.

It is demonstrated in the aforementioned references that this type of structure operates as an ultrabroadband room-temperature photodetector with intrinsic polarization sensitivity, through the photothermoelectic effect. The high degree of alignment in the film provides intrinsic polarization dependency due to the anisotropic absorption properties of CNTs. The broad polarization dependent absorption peak in the THz range is a property of aligned SWCNT films, resulting from intraband excitations in the individual one-dimensional SWCNTs and further enhanced by collective antenna effects in the macroscopically aligned film, as discussed in Section 4.2.2. While the p–n junction is not explicitly relevant for the purpose of this thesis, it is expected to contribute to the disorder of the sample in the low temperature regime.

5.2 Terahertz generation

In the experiments of this thesis, the device is illuminated by THz radiation produced by a molecular gas laser. The used laser setup consists of an Edinburgh model 295 far-infrared (FIR) laser, optically pumped by an Edinburgh Photonics PL5 flowing gas carbon dioxide (CO_2) laser. The latter produces single line powers up to 50 W and operates in over 80 discrete lines in a frequency range from 27.25 THz to 33.31 THz. With the two laser units combined, THz output power of 150 mW is available at frequencies of 2.52 THz and 1.63 THz. The full available output frequency range is from 0.25 THz to 7.49 THz.

The frequency used in the experiments of this thesis was chosen to be 2.52 THz for the highest output power. The 2.52 THz radiation is generated by optically pumping the FIR laser unit, filled with methanol (CH_3OH) gas, by 30.92 THz middle-infrared (MIR) range radiation. This MIR frequency is generated at the CO_2 laser with a specified maximum power of 45 W. The CO_2 laser uses a mixture of 75% helium (He), 18% diatomic nitrogen (N_2), and 7% CO_2 as the active medium. A plasma is generated inside the CO_2 gas tube by a high voltage DC source in order to excite the gas molecules and achieve population inversion.

The radiation inducing oscillation in the CO_2 laser takes place between two vibrational levels of CO_2, whereas He and N_2 are present to improve the efficiency of the lasing process. The vibrational energy levels of CO_2 and N_2 are shown in Figure 5.2a. N_2 is diatomic and, thus, has only one vibrational mode. In contrast, CO_2 is triatomic and has three nondegenerate vibrational modes: symmetrically stretching, symmetrically bending and antisymmetrically bending. The vibrational energy levels of CO_2 are described by three quantum numbers, n_1, n_2 and n_3, and the energy for each state is given by $E = n_1 h f_1 + n_2 h f_2 + n_3 h f_3$, where f_1, f_2 and f_3 are the frequencies of the three modes and h is the Planck's constant. Here, the zero-point energy of a harmonic oscillator is omitted. We denote these energy states as $n_1 n_2 n_3$. The lasing occurs from the pure asymmetrically stretching state

001 to one of the likewise single-moded states 100 or 020. The photon frequencies corresponding to the transition are 28.28 THz and 31.23 THz, from which the desired wavelength is picked by an optical grating. Pumping the 001 level of the CO_2 molecules is achieved by two processes: excitation by direct electron collisions and by resonant energy transfer from the excited N_2 molecules. The N_2 molecules are similarly excited through collisions with the high-energy electrons of the plasma inside the gas tube [60].

Methanol has an exceptionally rich energy state spectrum. Hence, the excitation dynamics of CH_3OH molecules is rather complex, and the detailed process for THz generation in methanol requires exhaustive quantum mechanical examination. Here, only the basic principle is presented. However, a more thorough investigation can be found, for instance, in Ref. [62]. A diagram of the process is depicted in Figure 5.2b. An incident photon from the CO_2 laser excites a transition between two vibrational states of the CH_3OH molecules. The energy of the 31 THz photon closely matches the energy separation of a particular rotational state in the lowest vibrational manifold and a rotational state in the first excited vibrational manifold. Given the right operating conditions, a population inversion is achieved between rotational states, either in the pumped excited vibrational manifold or in the lower manifold due to depletion of the lower state. In order to sustain the continuous-wave lasing process, the molecule has to then relax back to the lowest vibrational manifold to be excited again by the CO_2 laser [61].

As the energy difference between the vibrational manifolds in CH_3OH is large, most of the energy used for optical pumping is converted to heat. The theoretical limit for the efficiency, ϵ, of an optically pumped THz laser is given by the Manley–Rowe limit

$$\epsilon = \frac{v_{FIR}}{2v_{IR}}, \tag{5.1}$$

where v_{FIR} and v_{IR} denote the frequency of the emitted THz photons and the pumping frequency, respectively. Hence, the described process for generation of 2.5 THz photons has a theoretical limit of 4%. In practice, however, a typical efficiency is in the order of 0.2% [61].

5.3 Experimental setup

Two types of measurements were conducted in the experiments of this thesis. The first type was measuring the temperature dependence of resistance in the sample with and without THz illumination, and the second was the measurement of magnetoresistance in the CNT film without THz illumination. Nevertheless, the overall structure of the two measurement setups was the same, as shown in the schematic image in Figure 5.3. 2.52 THz radiation was produced as described in the previous section, and focused to an optical fibre by a plate mirror followed by a parabolic focusing mirror. Control over the laser power and polarization was achieved by setting up polarisers and filters between the focusing mirrors and the FIR modulating

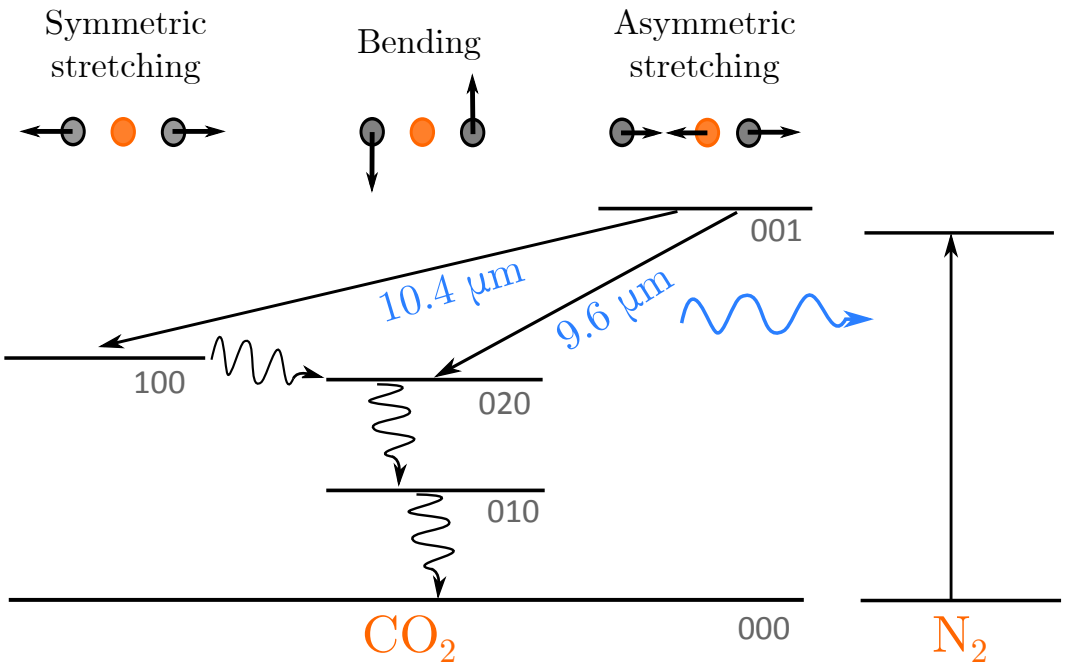

(a)

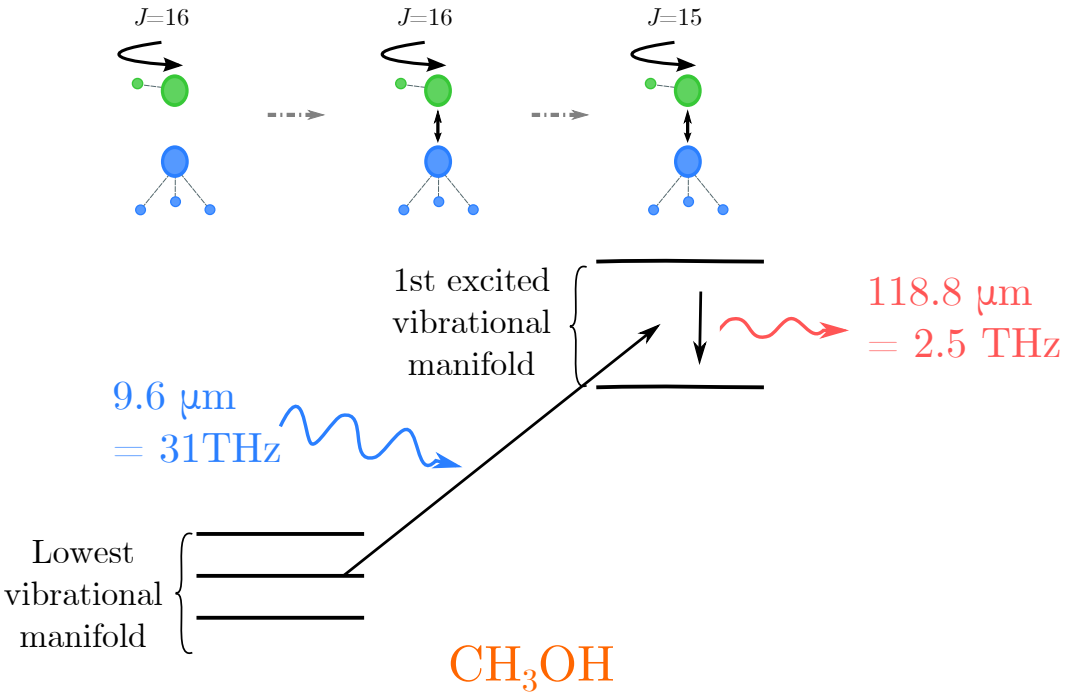

(b)

Figure 5.2: Excitation dynamics resulting in THz generation: Energy levels and transitions of a) CO_2 and N_2, adapted from [60], and b) CH_3OH, adapted from [61].

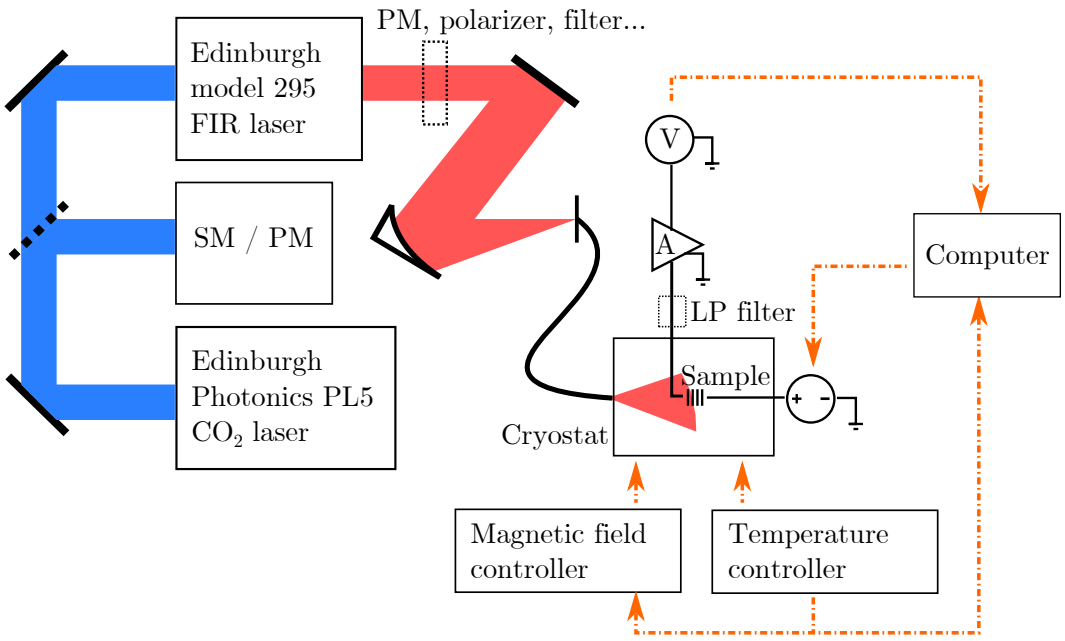

Figure 5.3: A schematic image of the measurement setup used in this thesis.

unit. The highly aligned SWCNT sample was mounted on a sample stage inside a ^{4}He flow-type cryostat, capable of reaching temperatures as low as ∼2.7 K. The sample was then illuminated by the optical fibre through a Tsurupica window, designed for high transparency in THz and visible spectral ranges. An additional black polyethylene filter was used to block out any visible light. The temperature of the cryostat was adjusted analogically using a controller, and the temperature reading from the sample stage was acquired digitally by a measurement program. A voltage was induced over the sample by an HP / Agilent 3245A power source and a current amplifier was set up between the sample and the multimeter in order to amplify the relatively weak current flowing through the sample. The amplifier converts current into voltage with a chosen sensitivity. Finally, the signal was collected as a voltage reading from an HP / Agilent 34401A digital multimeter.

The laser output power and the transmission rates of the optical components were measured using an Ophir Nova II power meter in combination with a thermal sensor. Transmission through the optical fibre was determined to be roughly 30%, which gradually decreased down to 4% at the ∼10 cm distance of the device inside the cryostat, due to spreading of the beam after the fibre. Additionally, transmission rates through the Tsurupica window and the polyethylene filter was determined to be 57.14% and 71.67% at 2.52 THz, respectively. Due to these notable power losses, the sample was expected to be illuminated by only ∼1–2% of the laser output power.

The details for different measurement types were as follows. For measuring the temperature dependence of resistance in the sample, the current amplifier sensitivity was set to be 10^{-7} A/V. The resistance was acquired by analysing I–V characteristics measured at every temperature point. Thus, a measurement program was set up to sweep the voltage and collect the data from the multimeter. The voltage was

swept from -10 mV to 10 mV to avoid Joule heating in the sample. For the magnetoresistance measurement setup an additional low-pass filter was added between the sample and the current amplifier. Furthermore, a higher sensitivity of 10^{-8} A/V was used for the current amplifier. Instead of a voltage sweep at every measurement point, a single voltage value of $V = 40$ mV was set on the power source to simplify the measurement. Higher voltage also provides increased sensitivity, as change in resistance results in greater change in current. The magnetic field source inside the cryostat was controlled with a measurement program.

6 Results and discussion

The results obtained from the experiments on the macroscopically aligned SWCNT p–n junction film are presented here in two parts. First, non-illuminated characteristics include a look on the I–V characteristics with different temperatures, the temperature dependence of resistance, $R(T)$, and the magnetoresistance, $\Delta R(B)/R_0$, in the sample. Second, illuminated characteristics cover the measurements of THz-induced change in resistance of the sample as a function of temperature, and the polarization and power dependencies of the photosignal. The data is analysed in terms of the theoretical concepts and previous research presented throughout this thesis, and the presentation of every set of results is followed by appropriate discussions.

6.1 Non-illuminated characteristics

Figure 6.1 shows the temperature dependence of resistance from room temperature down to approximately 2.9 K, as extracted from the measured I–V characteristics at every temperature point. Three examples of the linearly fitted I–V curves are also presented in Figure 6.1. The device shows linear I–V characteristics in the whole temperature range suggesting a good contact between the contacts and the sample. This also provides that the resistance of the sample can reliably be determined by the inverse slope of each I–V curve. While the offset current at $V = 0$ is due to the used current amplifier, it does not contribute to the resistance in the sample. Moreover, a relatively high noise can be observed at low temperatures. This is due to the fact that the increasing resistance approaches the detection limit of the measurement system.

It is immediately evident that the device exhibits a strongly nonlinear temperature dependence of resistance throughout the whole studied temperature range. To understand this trend, the data was analysed using the Mott model of variable-range hopping, following Eq. 3.18. As discussed in Section 3.3.1, d is the system dimension and T_0 is a characteristic temperature constant depending on the system, used here as a fitting parameter. The data is in excellent agreement with the Mott model at $T = 5$–200 K for $d = 2$. It is only at approximately $T = 3$–5 K that the data shows a deviation from the fitting function. All cases ($d = 1$, 2, and 3) were plotted also on an Arrhenius-type scale, as shown in the inset of Figure 6.1, where consistency with the VRH theory is expressed as linear dependence. Clearly, the two-dimensional ($d = 2$) VRH theory is in best agreement with the experimental data.

Variable-range hopping conduction is expected due to a high degree of disorder in the SWCNT sample. That is, the energy states in the device are expected to be strongly localized and, hence, the conduction is expected to be determined by tunnelling processes over varying distances. Random potential is expected to occur due to Schottky barriers between metallic and semiconducting SWCNTs, varying density of states due to statistically distributed nanotube diameters, and doping impurities. Additionally, hopping processes have also been observed in gallium nitride (GaN)

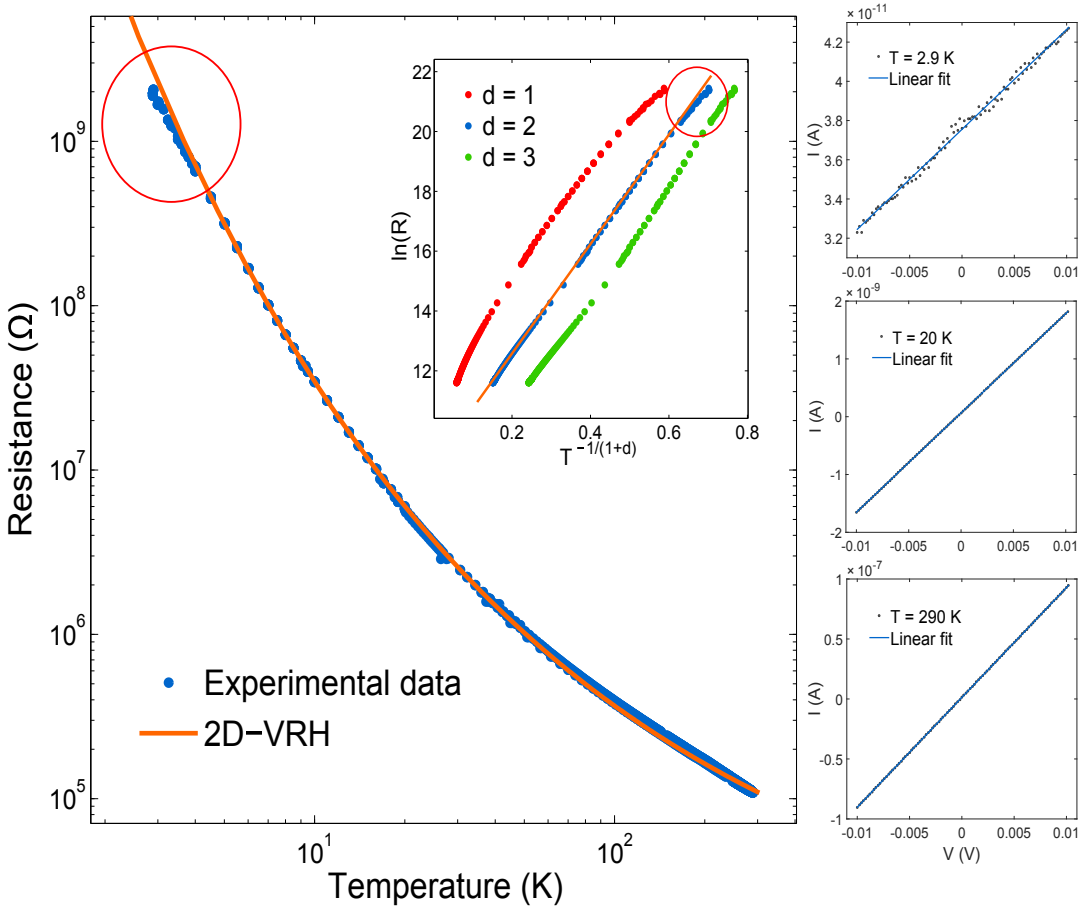

Figure 6.1: Temperature dependence of the resistance, obtained from I–V characteristics: Logarithmic scale and a fitting curve for two-dimensional VRH. Inset: Arrhenius type plot with $d = 1$, 2, and 3. The case $d = 2$ shows a linear dependency. Three examples of I–V curves, at T=2.9, 20 and 290 K, are also presented on the right.

p–n junctions, where, under reverse bias, electrons hop from the valence band of the p-type region through localized states in the depletion layer and finally tunnel to the conduction band of the n-type region [63, 64]. The dimensionality of the VRH mechanism is affected by the relative content of metallic SWCNTs, similarly to systems of conducting and insulating polymers, as well as the direction of the electronic transport relative to the nanotube alignment, as briefly reviewed in Chapter 4.2.

To investigate if the deviation from the fitting curve in Figure 6.1 can be interpreted as a crossover in conduction mechanism, the magnetoresistance of the sample was measured in the low temperature regime, as shown in Figure 6.2. Interestingly, the data clearly shows a low-field negative dip in magnetoresistance at temperatures $T = 3$–5 K, whereas purely positive MR is observed at temperatures $T = 7$–15 K. The turnover from negative to positive MR increases with temperature. Similarly,

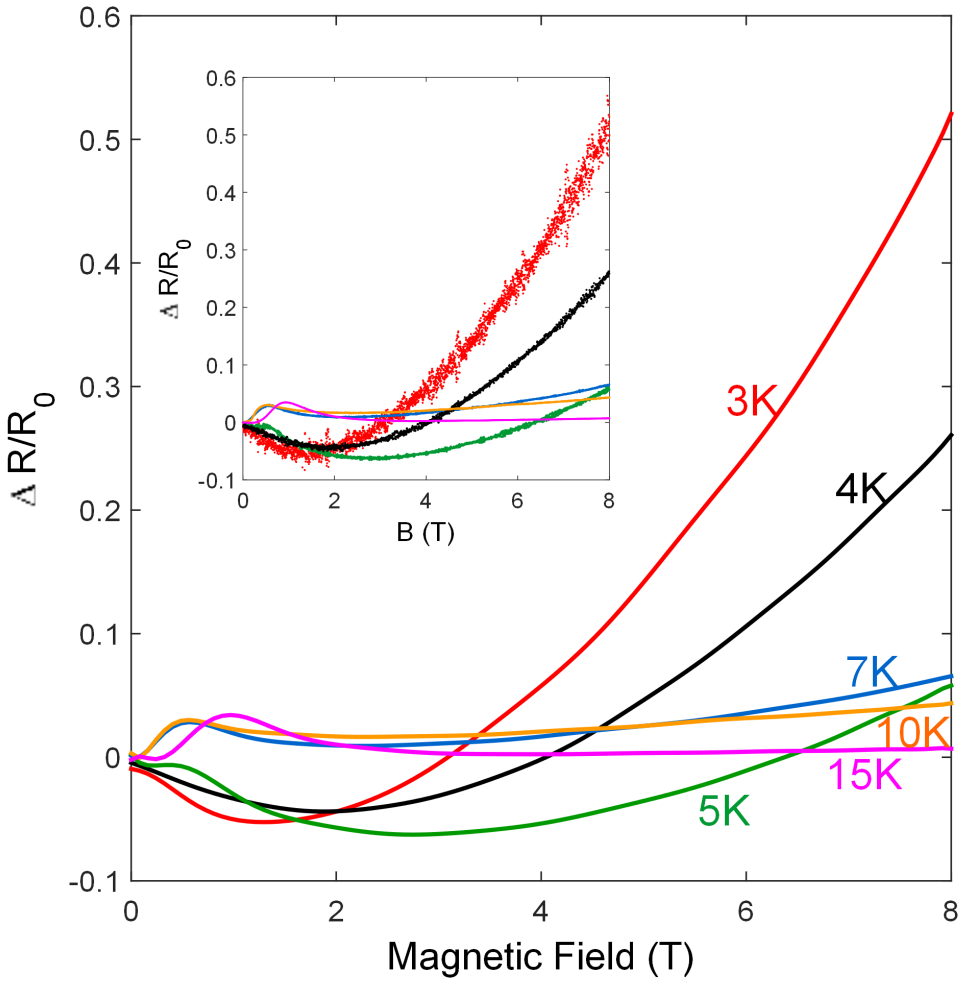

Figure 6.2: Fourier fitting curves for the measured magnetoresistances at $T = 3$, 4, 5, 7, 10, and 15 K. Inset: original data.

all curves show a positive slope at high magnetic fields, with decreasing saturation values as the temperature increases.

Section 3.3.3 introduced multiple theories predicting either positive or negative MR in the system expressing localization effects. The presence of both positive and negative MR could be interpreted to result from the coexistence of two distinct mechanisms. To test the hypothesis for simultaneous contributions from the weak localization (WL) and VRH mechanisms, the MR curve at $T = 3$ K was further analysed with the respective theories. The negative MR was analysed in the framework of two-dimensional weak localization theory (2D-WL) following the derived Eq. 3.55. Similarly, the positive contribution to the MR was fitted with Eq. 3.50 for Kurobe–Kamimura-type spin-dependent VRH (KK-VRH), as the observed decrease in the high-field saturation resistance with increasing temperature is consistent with the model. The two regimes were first analysed individually, separated at the mag-

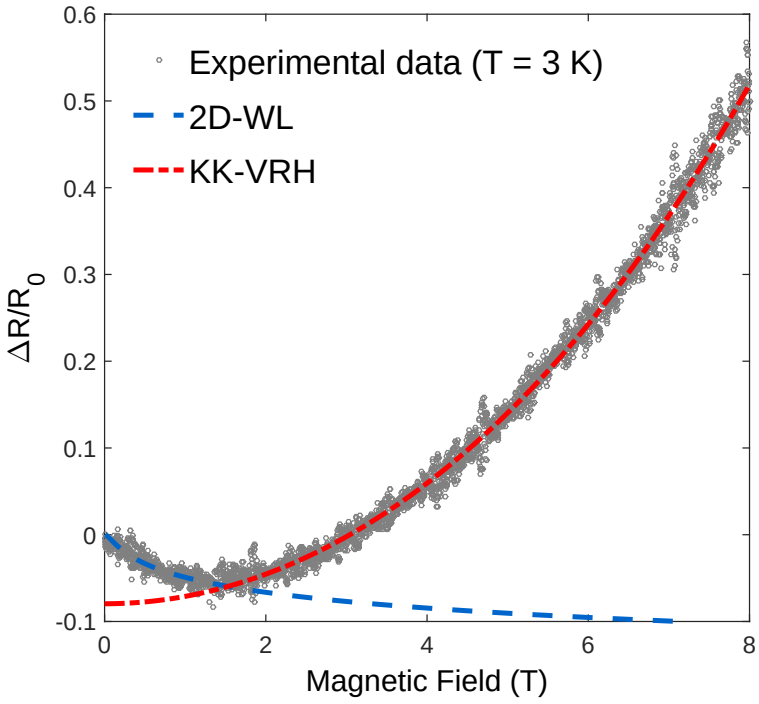

(a)

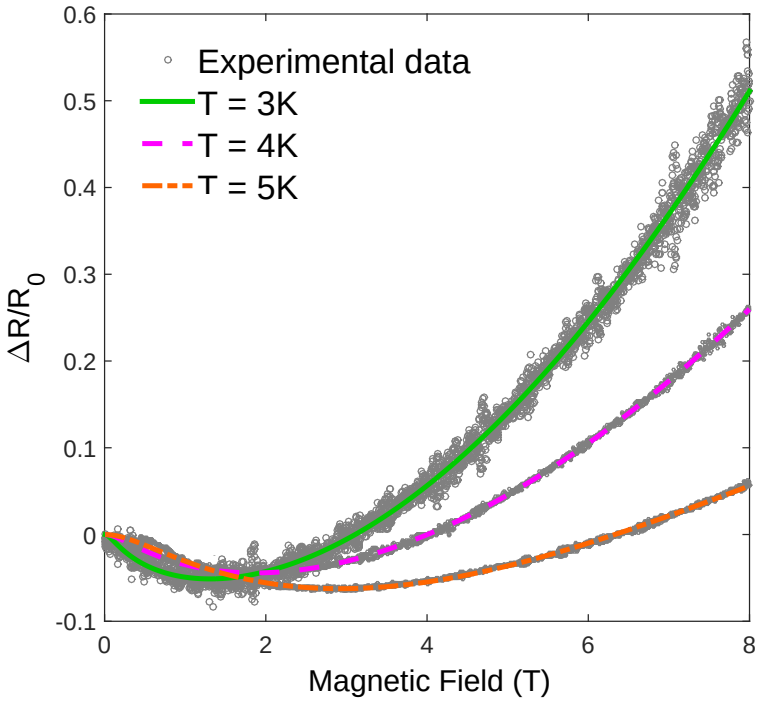

(b)

Figure 6.3: Fitting results for MR in terms of two-dimensional WL and Kurobe-Kamimura type VRH: a) Individual contributions from the mechanisms (KK-VRH offset to overlap with experimental data) and b) summed contributions at low T.

Table 6.1: The coherence length, L_ϕ, and the 95% confidence interval (CI) as extracted from the fitting results of magnetoresistance in the low temperature regime.

Temperature (K)	Coherence length (nm)	95% CI (nm)
3	63.1	[60.1; 66.7]
4	37.8	[37.1; 38.5]
5	27.3	[27.0; 27.7]

netic field value of the turnover from negative to positive MR. Following this, the full range was plotted as a sum of the two fitting functions. The functions reproduce the experimentally observed MR well, as can be seen from the fitting results presented in Figure 6.3a. The analysis was also repeated for the rest of the data sets that expressed negative MR with similar agreement, as depicted in Figure 6.3b. The observations agree with the interpretation of simultaneous transport mechanisms and point to the presence of weak localization in the device in the low-temperature limit.

The coherence lengths, L_ϕ, are extracted into Table 6.1 from the weak localization contribution in the fitting results of Figure 6.3. The coherence lengths are of the order tens of nanometers, decreasing strongly with increasing temperature. Both the length scale and the approximate temperature dependency ($L_\phi \simeq aT^{-p/2}$, with $p \approx 1$) are consistent with earlier work [49, 53]. The typical CNT diameter is of the order of a few nanometers. Hence, the relatively long coherence length may explain why the conduction is expressed in terms of a two-dimensional model, despite the relatively thick ($\sim$ 1 µm) SWCNT film of the device. The presence of both weak localization and Anderson localization provide an especially interesting setting to investigate the interplay between THz radiation and localization effects.

6.2 Illuminated characteristics

As the non-illuminated device revealed localization effects, it was next illuminated by low-energy, 2.52 THz radiation. The polarization of the THz radiation was chosen to be parallel to the nanotube alignment direction. The illuminated measurements were expected to reveal information about the interplay between localization effects and THz radiation. Figure 6.4 depicts the resistance of the illuminated device as a function of temperature. THz illumination induces a clear resistance difference, as strong as ∼55% at 3 K with the chosen laser output intensity of 20 mW, up to a temperature of approximately 15 K. To further illustrate the photoresponse, also the power dependence of the signal was measured and is shown in Figure 6.5a. Based on the power dependence fitting curve and further considering the low transmission rate (∼1–2%) of the measurement system, even a modest incident intensity of ∼1 mW induces a relative resistance change of over 80% in the device.

The photosignal can originate from various mechanisms, as discussed in Section 4.2.2. The photothermoelectric effect can be neglected, as it does not affect the resistance in the device. However, distinguishing between phonon- and photon-induced

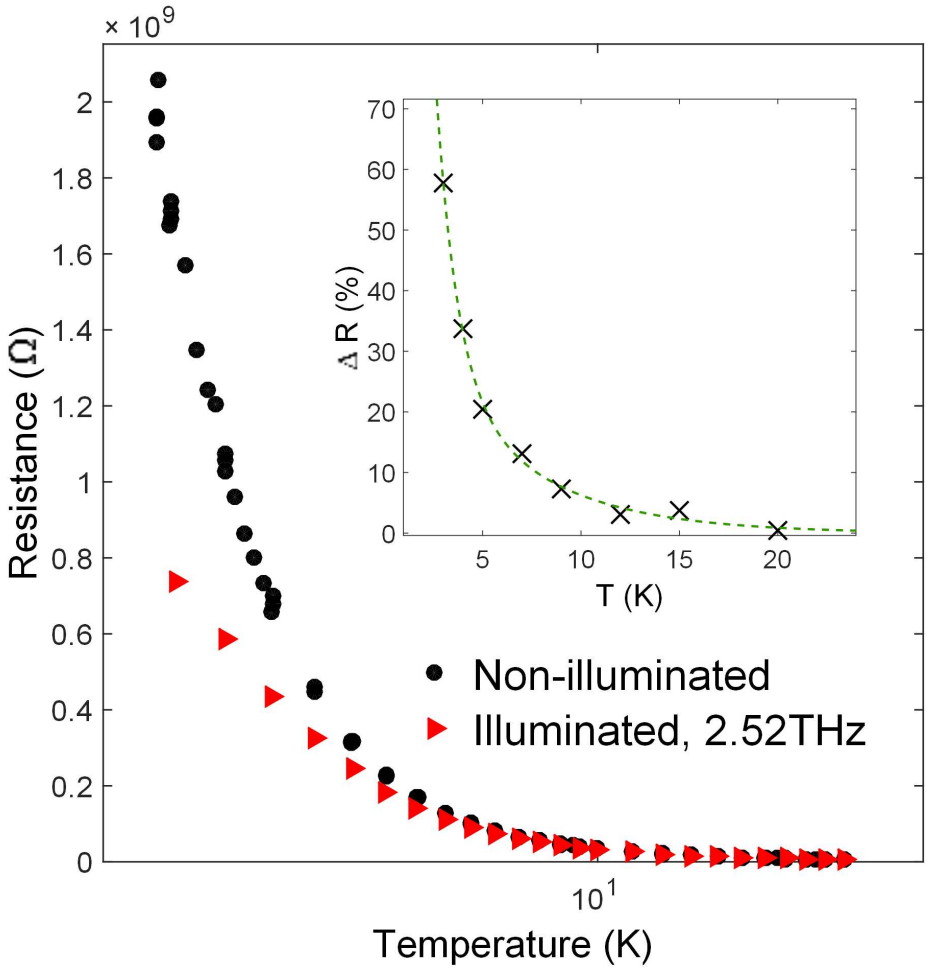

Figure 6.4: The temperature dependence of resistance in the sample in the presence and in the absence of 2.52 THz illumination. Inset: relative decrease in the resistance due to THz illumination as a function of temperature.

tunnelling processes requires some additional care. The difference is measurable in two ways. The first way is to measure the photosignal in time-domain. Phonon-assisted tunnelling is mediated by lattice heating, which is a relatively slow process as compared to photon induced tunnelling, which does not require a medium. The second method to measure the difference is exploiting the strongly polarization dependent absorptivity of the highly aligned SWCNT sample. Phonon-induced tunnelling is absorption dependent and should show strong polarization dependence. Photon-induced tunnelling is expected to be unaffected by the polarization of the incident THz radiation.

To confirm the origin of the photosignal, the device was illuminated with 0° and 90° polarizations, relative to the SWCNT orientation. Due to the strongly polarization sensitive absorption properties of the highly aligned carbon nanotube network, these measurements are expected to reveal information about the absorption dependence

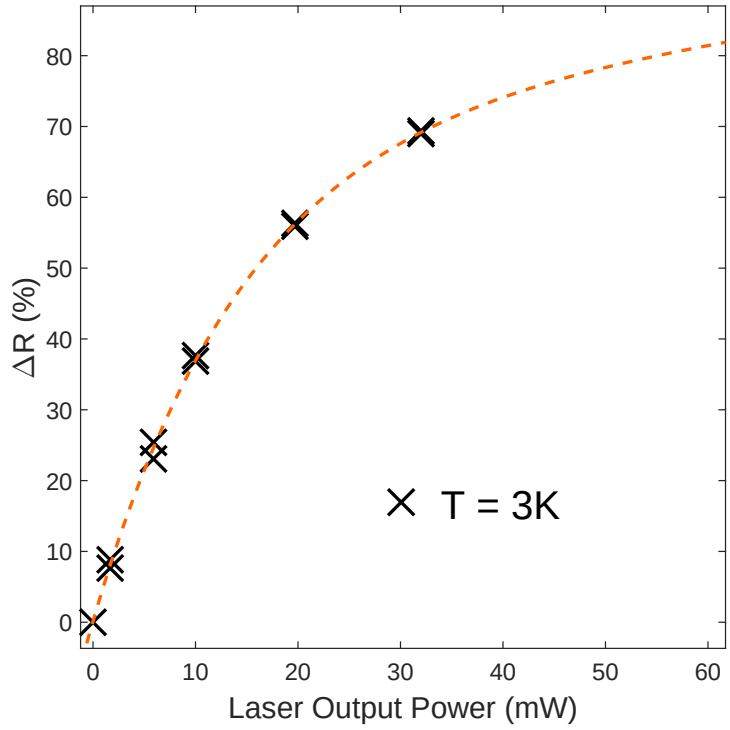

(a)

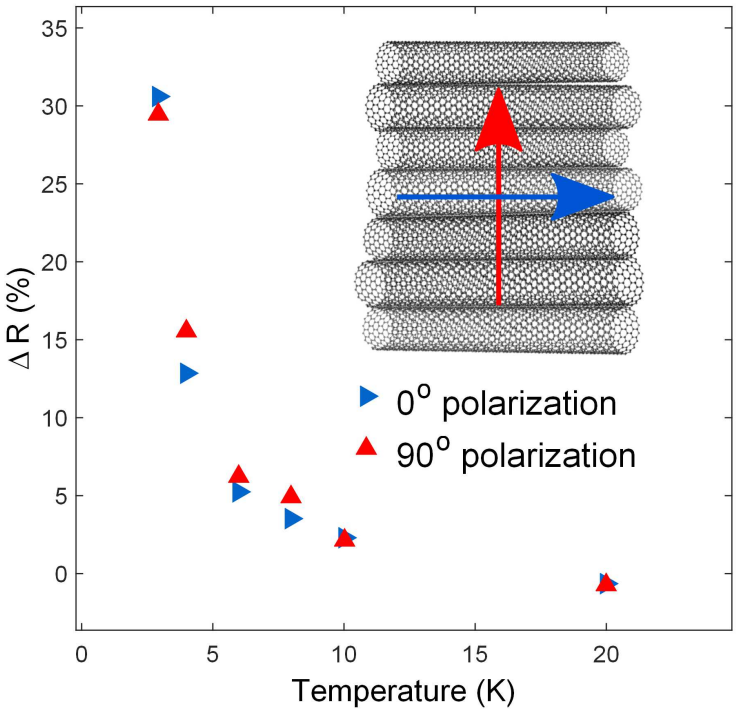

(b)

Figure 6.5: The resistance change in the THz-illuminated device as a function a) laser output power and b) temperature for perpendicular polarizations.

of the photoresponse. A lower laser intensity of 4 mW was used in the polarization dependence measurement, since the output intensity of the used laser setup is considerably lower for the 90° polarization. The same intensity for the 0° polarization was obtained by the use of optical filters. The produced data is presented in Figure 6.5b. Both polarizations show a strong photoresponse, and it is revealed that the two perpendicular polarizations show no distinct difference in the magnitude of the response. Thus, the data points to the conclusion that the detected signal is not of bolometric nor photothermoelectric origin. The THz photoconductance can thus be attributed to THz photon assisted tunnelling of electrons between localized hopping sites. The result further introduces the interesting possibility that THz illumination influences the single-electron interference originated coherent backscattering effect in the presence of weak localization.

7 Conclusions

In summary, this thesis studied the electronic transport in a highly aligned single-wall carbon nanotube p–n junction film and investigated the photoconductivity of the device under 2.52 THz illumination. The literature part of the thesis derived some of the basic concepts of mesoscopic physics, including an elaborate investigation on the theory of localization. The theoretical results were then exploited for analysing the transport characteristics of the SWCNT film.

The temperature dependence of resistance in the device showed clear evidence of two-dimensional Mott variable-range hopping down to approximately 5 K, where a deviation from theoretical curve was observed. The magnetoresistance measurements showed a similar crossover and characteristics of weak localization, classified as quantum transport. The device exhibited a strong polarization-independent THz photoconductivity response, established to originate from THz photon-assisted tunnelling processes between localized hopping sites. The strong low temperature response may further result from the influence of the THz radiation on weak localization.

The observations demonstrate the potential of THz radiation for probing the properties of complex mesoscopic systems and light way for new sophisticated strategies for THz detection. While the photosignal was restricted to an investigated temperature region of $T = 3$–20 K, limiting its practical utilizability for THz detection, the results give insight into the transport phenomena in complex systems. While understanding the underlying interactions is important for various potential device applications of SWCNT films, the observations also represent features of complicated mesoscopic systems in a more general sense.

To point out some plausible sources for error in the measurements, it is noteworthy that the MR measurements were conducted by measuring the output current with a single voltage value to simplify the measurement. As the current amplifier is expected to add a constant offset to the output current (see, e.g., Figure 6.1), it may induce some error to the MR data. However, as MR is calculated as the relative change in resistance as a function of magnetic field, the overall quality of the data suggests this error to be negligible, mostly affecting the already approximative localization lengths in Table 6.1. Moreover, the measured temperature readings in all data sets were measured from sample stage inside the cryostat. Hence, it is possible that during a measurement the device and the sample stage are at different temperatures as the THz radiation heats up the device. However, this error should have also produced a polarization dependent photosignal, as the temperature difference between the sample and the stage depends on the absorptivity of the CNT film.

Despite ever increasing interest in THz technology and continuous investigation of the transport phenomena in CNTs, only few studies have been conducted to investigate the relation between the two. Hence, further research is required to understand the full picture of such complicated systems. Frequency-domain measurement is expected to reveal further information about the photoresponse. Furthermore, as

the data does not explicitly reveal information about the interaction between weak localization and THz radiation, a time-domain measurement could potentially distinguish between effects originating from weak localization and variable-range hopping. Such an approach has already been used [46, 47] to distinguish between effects arising from bolometric and photon-induced tunnelling origins, since the time scales of the effects are fundamentally different.

References

[1] P. W. Anderson *et al.*, "More is different," *Science*, vol. 177, no. 4047, pp. 393–396, 1972.

[2] P. W. Anderson, "Absence of diffusion in certain random lattices," *Phys. Rev.*, vol. 109, pp. 1492–1505, 1958.

[3] D. S. Wiersma, P. Bartolini, A. Lagendijk, and R. Righini, "Localization of light in a disordered medium," *Nature*, vol. 390, no. 6661, pp. 671–673, 1997.

[4] A. Chabanov, M. Stoytchev, and A. Genack, "Statistical signatures of photon localization," *Nature*, vol. 404, no. 6780, pp. 850–853, 2000.

[5] H. Hu, A. Strybulevych, J. Page, S. E. Skipetrov, and B. A. van Tiggelen, "Localization of ultrasound in a three-dimensional elastic network," *Nature Physics*, vol. 4, no. 12, pp. 945–948, 2008.

[6] J. Chabé, G. Lemarié, B. Grémaud, D. Delande, P. Szriftgiser, and J. C. Garreau, "Experimental observation of the anderson metal-insulator transition with atomic matter waves," *Physical review letters*, vol. 101, no. 25, p. 255702, 2008.

[7] A. Lagendijk, B. van Tiggelen, and D. S. Wiersma, "Fifty years of anderson localization," *Phys. Today*, vol. 62, no. 8, pp. 24–29, 2009.

[8] J.-C. Charlier, X. Blase, and S. Roche, "Electronic and transport properties of nanotubes," *Reviews of modern physics*, vol. 79, no. 2, p. 677, 2007.

[9] A. Javey, J. Guo, Q. Wang, M. Lundstrom, and H. Dai, "Ballistic carbon nanotube field-effect transistors," *Nature*, vol. 424, no. 6949, pp. 654–657, 2003.

[10] T. Fuse, Y. Kawano, T. Yamaguchi, Y. Aoyagi, and K. Ishibashi, "Quantum response of carbon nanotube quantum dots to terahertz wave irradiation," *Nanotechnology*, vol. 18, no. 4, p. 044001, 2007.

[11] M. Bockrath, D. H. Cobden, J. Lu, A. G. Rinzler, R. E. Smalley, L. Balents, and P. L. McEuen, "Luttinger-liquid behaviour in carbon nanotubes," *Nature*, vol. 397, no. 6720, pp. 598–601, 1999.

[12] M. Engel, J. P. Small, M. Steiner, M. Freitag, A. A. Green, M. C. Hersam, and P. Avouris, "Thin film nanotube transistors based on self-assembled, aligned, semiconducting carbon nanotube arrays," *ACS Nano*, vol. 2, no. 12, pp. 2445–2452, 2008.

[13] Z. Wu, Z. Chen, X. Du, J. M. Logan, J. Sippel, M. Nikolou, K. Kamaras, J. R. Reynolds, D. B. Tanner, A. F. Hebard, *et al.*, "Transparent, conductive carbon nanotube films," *Science*, vol. 305, no. 5688, pp. 1273–1276, 2004.

[14] Q. Cao and J. A. Rogers, "Ultrathin films of single-walled carbon nanotubes for electronics and sensors: A review of fundamental and applied aspects," *Advanced Materials*, vol. 21, no. 1, pp. 29–53, 2009.

[15] T. Kampfrath, K. Tanaka, and K. A. Nelson, "Resonant and nonresonant control over matter and light by intense terahertz transients," *Nature Photonics*, vol. 7, no. 9, pp. 680–690, 2013.

[16] Y. Kawano, "Terahertz waves: a tool for condensed matter, the life sciences and astronomy," *Contemporary Physics*, vol. 54, no. 3, pp. 143–165, 2013.

[17] M. Tonouchi, "Cutting-edge terahertz technology," *Nature Photonics*, vol. 1, no. 2, pp. 97–105, 2007.

[18] D. M. Mittleman, "Frontiers in terahertz sources and plasmonics," *Nature Photonics*, vol. 7, no. 9, pp. 666–669, 2013.

[19] S. Datta, *Quantum transport: atom to transistor*. Cambridge University Press, 2005.

[20] Y. Imry, *Introduction to mesoscopic physics*. Oxford Univ. Press, 1997.

[21] S. Datta, *Electronic transport in mesoscopic systems*. Cambridge Studies in Semiconductor Physics and Microelectronic Engineering, Cambridge University Press, 1997.

[22] D. Ferry and S. Goodnick, *Transport in nanostructures*. Cambridge studies in semiconductor physics and microelectronic engineering, Cambridge University Press, 1997.

[23] S. Datta, *Lessons from nanoelectronics: a new perspective on transport*. Lessons from nanosciences: A lecture note series, Singapore: World Scientific, 2012.

[24] N. F. Mott and E. A. Davis, *Electronic processes in non-crystalline materials*. Oxford University Press, 1979.

[25] P. A. Lee and T. Ramakrishnan, "Disordered electronic systems," *Reviews of Modern Physics*, vol. 57, no. 2, p. 287, 1985.

[26] P. Wölfle and D. Vollhardt, "Self-consistent theory of anderson localization: General formalism and applications," *International Journal of Modern Physics B*, vol. 24, no. 12n13, pp. 1526–1554, 2010.

[27] D. J. Thouless, "Electrons in disordered systems and the theory of localization," *Physics Reports*, vol. 13, no. 3, pp. 93–142, 1974.

[28] E. Abrahams, P. Anderson, D. Licciardello, and T. Ramakrishnan, "Scaling theory of localization: absence of quantum diffusion in two dimensions," *Physical Review Letters*, vol. 42, no. 10, pp. 673–676, 1979.

[29] F. J. Wegner, "Electrons in disordered systems. scaling near the mobility edge," *Zeitschrift für Physik B Condensed Matter*, vol. 25, no. 4, pp. 327–337, 1976.

[30] N. Mott, *Conduction in non-crystalline materials*. Oxford science publications, Clarendon Press, 1987.

[31] A. Efros and B. Shklovskii, "Coulomb gap and low temperature conductivity of disordered systems," *Journal of Physics C: Solid State Physics*, vol. 8, no. 4, p. L49, 1975.

[32] A. Efros and B. Shklovskii, "Electronic properties of doped semiconductors," *Springer Series in Solid-State Sciences, Springer, Berlin*, 1984.

[33] B. Kramer and A. MacKinnon, "Localization: theory and experiment," *Reports on Progress in Physics*, vol. 56, no. 12, p. 1469, 1993.

[34] A. Kurobe and H. Kamimura, "Correlation effects on variable range hopping conduction and the magnetoresistance," *Journal of the Physical Society of Japan*, vol. 51, no. 6, pp. 1904–1913, 1982.

[35] A. Frydman and Z. Ovadyahu, "Spin and quantum interference effects in hopping conductivity," *Solid state communications*, vol. 94, no. 9, pp. 745–749, 1995.

[36] V. Nguyen, B. Spivak, and B. Shklovskii, "Aaronov-bohm oscillations with normal and superconducting flux quanta in hopping conductivity," *JETP Lett*, vol. 41, no. 1, 1985.

[37] V. Nguen, B. Spivak, and B. Shklovskii, "Tunnel hopping in disordered systems," *Zh. Eksp. Teor. Fiz*, vol. 89, pp. 1770–1784, 1985.

[38] U. Sivan, O. Entin-Wohlman, and Y. Imry, "Orbital magnetoconductance in the variable-range–hopping regime," *Physical review letters*, vol. 60, no. 15, p. 1566, 1988.

[39] O. Entin-Wohlman, Y. Imry, and U. Sivan, "Orbital magnetoconductance in the variable-range-hopping regime," *Physical Review B*, vol. 40, no. 12, p. 8342, 1989.

[40] S. Hikami, A. I. Larkin, and Y. Nagaoka, "Spin-orbit interaction and magnetoresistance in the two dimensional random system," *Progress of Theoretical Physics*, vol. 63, no. 2, pp. 707–710, 1980.

[41] P. L. McEuen, M. S. Fuhrer, and H. Park, "Single-walled carbon nanotube electronics," *IEEE transactions on nanotechnology*, vol. 1, no. 1, pp. 78–85, 2002.

[42] M. Anantram and F. Leonard, "Physics of carbon nanotube electronic devices," *Reports on Progress in Physics*, vol. 69, no. 3, p. 507, 2006.

[43] B. Gharekhanlou and S. Khorasani, "An overview of tight-binding method for two-dimensional carbon structures," *Graphene: Properties, Synthesis and Application*, pp. 1–37, 2011.

[44] A. Javey and J. Kong, *Carbon nanotube electronics*. Springer, 2009.

[45] P. N. Nirmalraj, P. E. Lyons, S. De, J. N. Coleman, and J. J. Boland, "Electrical connectivity in single-walled carbon nanotube networks," *Nano letters*, vol. 9, no. 11, pp. 3890–3895, 2009.

[46] V. Ksenevich, V. Odzaev, Z. Martunas, D. Seliuta, G. Valusis, J. Galibert, A. Melnikov, A. Wieck, D. Novitski, M. Kozlov, *et al.*, "Localization and nonlinear transport in single walled carbon nanotube fibers," *Journal of Applied Physics*, vol. 104, no. 7, p. 073724, 2008.

[47] D. Seliuta, I. Kašalynas, J. Macutkevic, G. Valušis, M. V. Shuba, P. P. Kuzhir, G. Y. Slepyan, S. A. Maksimenko, V. K. Ksenevich, V. Samuilov, *et al.*, "Terahertz sensing with carbon nanotube layers coated on silica fibers: Carrier transport versus nanoantenna effects," *Applied Physics Letters*, vol. 97, no. 7, p. 073116, 2010.

[48] P. Sheng, "Fluctuation-induced tunneling conduction in disordered materials," *Physical Review B*, vol. 21, no. 6, p. 2180, 1980.

[49] K. Yanagi, H. Udoguchi, S. Sagitani, Y. Oshima, T. Takenobu, H. Kataura, T. Ishida, K. Matsuda, and Y. Maniwa, "Transport mechanisms in metallic and semiconducting single-wall carbon nanotube networks," *ACS Nano*, vol. 4, no. 7, pp. 4027–4032, 2010.

[50] M. Reghu, C. Yoon, C. Yang, D. Moses, P. Smith, A. Heeger, and Y. Cao, "Transport in polyaniline networks near the percolation threshold," *Physical Review B*, vol. 50, no. 19, p. 13931, 1994.

[51] J. Planès, A. Wolter, Y. Cheguettine, A. Proń, F. Genoud, and M. Nechtschein, "Transport properties of polyaniline-cellulose-acetate blends," *Physical Review B*, vol. 58, no. 12, p. 7774, 1998.

[52] C. L. Pint, Y.-Q. Xu, E. Morosan, and R. H. Hauge, "Alignment dependence of one-dimensional electronic hopping transport observed in films of highly aligned, ultralong single-walled carbon nanotubes," *Applied Physics Letters*, vol. 94, no. 18, p. 182107, 2009.

[53] G. Kim, E. Choi, D. Kim, D. Suh, Y. Park, K. Liu, G. Duesberg, and S. Roth, "Magnetoresistance of an entangled single-wall carbon-nanotube network," *Physical Review B*, vol. 58, no. 24, p. 16064, 1998.

[54] Q. Zhang, E. H. Hároz, Z. Jin, L. Ren, X. Wang, R. S. Arvidson, A. Lüttge, and J. Kono, "Plasmonic nature of the terahertz conductivity peak in single-wall carbon nanotubes," *Nano letters*, vol. 13, no. 12, pp. 5991–5996, 2013.

[55] L. Ren, Q. Zhang, C. Pint, A. Wójcik, M. Bunney Jr, T. Arikawa, I. Kawayama, M. Tonouchi, R. Hauge, A. Belyanin, *et al.*, "Collective antenna effects in the terahertz and infrared response of highly aligned carbon nanotube arrays," *Physical Review B*, vol. 87, no. 16, p. 161401, 2013.

[56] X. He, N. Fujimura, J. M. Lloyd, K. Erickson, Q. Zhang, W. Gao, Q. Jiang, Y. Kawano, R. H. Hauge, F. Leonard, *et al.*, "Carbon nanotube terahertz detector," *Nano letters*, 2014.

[57] S. Nanot, A. W. Cummings, C. L. Pint, A. Ikeuchi, T. Akiho, K. Sueoka, R. H. Hauge, F. Léonard, and J. Kono, "Broadband, polarization-sensitive photodetector based on optically-thick films of macroscopically long, dense, and aligned carbon nanotubes," *Scientific reports*, vol. 3, 2013.

[58] X. He, X. Wang, S. Nanot, K. Cong, Q. Jiang, A. A. Kane, J. E. Goldsmith, R. H. Hauge, F. Léonard, and J. Kono, "Photothermoelectric p–n junction photodetector with intrinsic broadband polarimetry based on macroscopic carbon nanotube films," *ACS Nano*, vol. 7, no. 8, pp. 7271–7277, 2013.

[59] C. L. Pint, Y.-Q. Xu, S. Moghazy, T. Cherukuri, N. T. Alvarez, E. H. Haroz, S. Mahzooni, S. K. Doorn, J. Kono, M. Pasquali, *et al.*, "Dry contact transfer printing of aligned carbon nanotube patterns and characterization of their optical properties for diameter distribution and alignment," *ACS Nano*, vol. 4, no. 2, pp. 1131–1145, 2010.

[60] O. Svelto and D. Hanna, *Principles of Lasers*. Springer, 1998.

[61] E. R. Mueller, "Optically-pumped thz laser technology," *Coherent-DEOS product Note*, pp. 1–10, 2001.

[62] E. R. Mueller, "Submillimeter wave lasers," *Wiley Encyclopedia of Electrical and Electronics Engineering*, 1999.

[63] D. Kuksenkov, H. Temkin, A. Osinsky, R. Gaska, and M. Khan, "Low-frequency noise and performance of gan pn junction photodetectors," *Journal of applied physics*, vol. 83, no. 4, pp. 2142–2146, 1998.

[64] E. Miller, E. Yu, P. Waltereit, and J. Speck, "Analysis of reverse-bias leakage current mechanisms in gan grown by molecular-beam epitaxy," *Applied physics letters*, vol. 84, no. 4, pp. 535–537, 2004.